POLITECNICO DI MILANO

Facoltà di Ingegneria dei Sistemi

Corso di Laurea in Ingegneria Fisica

RAMAN INDUCED KERR EFFECT SPECTROSCOPY FOR LABEL-FREE MOLECULE DETECTION

Supervisor: Giulio Cerullo

Co-supervisor: Marco Marangoni

Experimental thesis of Master Degree of:

Filippo Campi

N. 733911

Academic Year 2010-2011

Contents

TABLE OF FIGURES

ABSTRACT

La tesi verte sullo sviluppo di un innovativo apparato di microscopia Raman coerente basato un oscillatore laser in fibra munito di tre stadi di amplificazione ed altrettante uscite, che offre un vantaggio significativo rispetto ai sistemi laser attualmente utilizzati in termini di compatezza e versatilità. Tale apparato sperimentale è stato applicato con successo in esperimenti di spettroscopia vibrazionale coerente su diversi tipi di campione, nelle configurazioni CARS (Coherent Anti-Stokes Raman Spectroscopy), SRS (Stimulated Raman Scattering) e anche sulla più innovativa tecnica RIKES (Raman-Induced Kerr-Effect Spectroscopy). Si è dimostrato che quest'ultima, pur di utilizzare l'apparato in combinazione con una rivelazione bilanciata e un controllo della polarizzazione, risulta estremamente competitiva, in quando non presenta il background non risonante tipico del CARS e nello stesso tempo supera l'SRS nel rapporto segnale rumore. I risultati ottenuti suggeriscono che la tecnica proposta possa essere perfezionata e successivamente applicata per investigare campioni più complessi, quali campioni di interesse biologico o biomedico. Nella stessa tesi, prima di presentare i risultati sperimentali ottenuti, si sono ampiamente analizzati matematicamente i fenomeni non lineari che prendono parte ai processi sfruttati così come si sono approfonditi alcuni aspetti tecnologici riguardanti l'apparato sperimentale utilizzato in laboratorio.

ABSTRACT

This thesis concerns developing an innovative coherent Raman microscopy setup, based on a fiber oscillator connected to three amplifiers and with three outputs. It is an advantage compared to traditionally-used setups in terms of compactness, cost-efficiency, and versatility. Such a setup has been successfully applied on coherent vibrational spectroscopy experiments on various samples, in different configurations: CARS (Coherent Anti-Stokes Spectroscopy), SRS (Stimulated Raman Scattering), and on the most recent RIKES (Raman-Induced Kerr Effect Spectroscopy). It has been proved that RIKES, when combined with the balanced detection and a polarization control, is extremely competitive, not having the typical CARS non-resonant background, and at the same time granting a better signal to noise ratio than SRS. Obtained results suggest the chance to improve the implementation of the technique in order to investigate biological or biomedical samples. In the thesis, before presenting experimental results obtained, non-linear phenomena that take place in the exploited processes are vastly mathematically treated, as well as some of the technological aspects of the experimental setup used in the laboratory were discussed.

INTRODUCTION

The development of optical microscopy has radically changed our ability to investigate the microscopic world. Nonetheless every optical microscopy technique, from the easiest to the more complicated ones such as phase contrast microscopy, although fundamental in probing biological tissues, has a scarce chemical selectivity. Other optical microscopy techniques, for instance fluorescence microscopy, permit to identify specific molecules, but on the other hand they require fluorescent markers in order to obtain an image. These markers may alter significantly the system to be probed, mainly when analyzing small molecular samples.

Vibrational microscopy represents a valid option to overcome this problem. It allows molecule identification based on the characteristic vibrational response of these. Among others, Raman microscopy has been applied in many fields, mainly in biomedical applications. However its sensitivity is highly curbed by the low efficiency of the spontaneous Raman scattering and this prevents from analyzing in vivo samples and from acquiring images with high frame-rate. It also needs high power laser sources, which often would damage the probed system.

In this background, starting from the 90s, new vibrational techniques have been developed and are still being improved, based on coherent Raman processes, such as Coherent Raman Anti-Stokes Scattering (CARS), Stimulated Raman Scattering (SRS), Raman Induced Kerr Effect Scattering (RIKES), and many others. These techniques generate much higher signals and make possible to analyze in vivo samples and video-rate acquisition. The effects upon which CARS, SRS and RIKES are based have been demonstrated many years ago, and these techniques have been used for spectro-microscopy purposes in the investigation of biological tissues and gases. Nowadays these techniques are mainly used in few advanced laboratories, because of the bulky and expensive setups needed, such as Ti:shappire lasers or Optical Parametric Oscillators (OPOs).

The experimental work that served as the basis for this thesis concerned designing and building a brand new setup for Coherent Raman spectroscopy/microscopy experiments as well as implementing an alternative detection scheme for RIKES experiments. The setup, which was more compact and cost-effective compared to the currently used ones, and it was based on a femtosecond fiber laser which exploited a recently demonstrated spectral compression technique to produce narrowband tunable picosecond pulses. At the same time it offered the unprecedented capability of permit several coherent Raman spectroscopy configurations, such as single colour or multiplex CARS/SRS, as well as many different background-suppression techniques. In particular a new configuration has been developed, based on the RIKES process. Such a process, combined with a balanced detection and a polarization control allowed us to achieve results close to the state of the art.

The thesis is divided into four chapters, whose content are subsequently summarized:

Chapter 1 is a theoretical introduction to light-matter interaction processes, and particularly to phenomena that give rise to CARS and SRS signals; these two techniques were, in fact, used to start the setup and to run first experiments. The last paragraph presents some of the results that could be found in recent papers.

In Chapter 2 two different approaches to the RIKES signal detection are described, as well as a brief theoretical argument leading to the expression of the signal to be detected. Afterwards the solution adopted during the experiments will be discussed, before presenting some results of the state of the art of RIKES.

Chapter 3 contains all the details about the laser system, the spectral compression technique used to convert femtosecond pulses to picosecond ones, and the setup built and used for these experiments.

In Chapter 4 CARS/SRS/RIKES spectroscopy results on solvent samples and SRS/RIKES microscopy on polysterene samples will be presented and discussed.

Appendixes A and B give an insight of third order non-linear processes and of light interaction with the detection scheme used in RIKES experiments.

CHAPTER 1

Coherent Raman Spectroscopy techniques: CARS-SRS

In this chapter the two most well-known and widely studied *coherent Raman spectroscopy (CRS*) techniques will be presented: CARS and SRS. They share the main idea of exploiting the nonlinear response of the material in order to obtain much higher signals compared to those that arise from linear response, which is typically exploited in classic Raman spectroscopy. It's possible to show that the radiation generated by these non-linear processes is coherent, thus easier and faster measurements are allowed, and with a better signal to noise ratio.

The classical spontaneous Raman spectroscopy probes the vibrational transition through a linear absorption process. Starting from the ground state an incident photon with frequency ω_p induces a transition from the ground state to a virtual state. Due to a spontaneous decay a photon is generated with frequency $(\omega_p-\Omega)$, where $\hbar\Omega$ is the energy difference between the ground state and the vibrational level to be probed, corresponding to the vibrational

transition energy. This kind of spectroscopy allows to access to low energy transitions, corresponding to low energy quanta, generally in the infrared region, using only visible light. Usually the transition induced by the absorbed photon is not resonant, and this leads to very low conversion efficiency, on the order of 10^{-18}. Furthermore this process results in a spontaneous scattering, which is isotropic and thus the detected intensity is only a small fraction of the overall intensity causing this process to be highly inefficient[1]. In Fig.1.1a the spontaneous Raman scattering is shown.

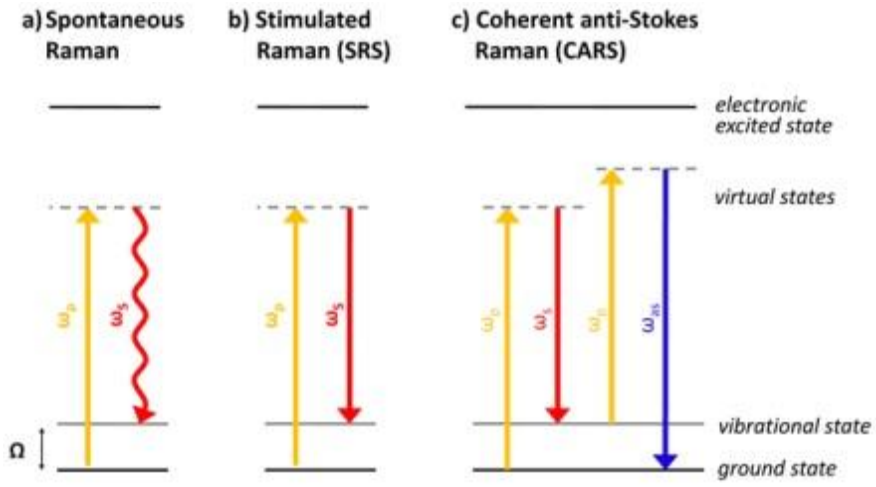

Fig.1.1 Energy levels involved in spontaneous Raman scattering (a), in SRS (b), and in CARS (c)

Both CARS and SRS processes are based on third order effects, thus not only two, but four photons are interacting. This way the generated photon is carrying information regarding the frequency, polarization, phase, and magnitude of the non-linear interaction between the three input fields. In Fig.1.1c the energy levels involved in the CARS process are represented; this diagram clearly points out the four-photon nature of such a process. Fig.1.1b represents the SRS process which is a four-photon one as well, although a

degenerate one; in fact, two photons per each frequency represented are interacting to generate the signal.

In each of these non-linear spectroscopies, when the frequency difference is tuned in order that it matches the vibrational frequency, the signal wave is highly enhanced, indicating the Raman resonance. In addition, as a result of the coherent nature of the process, the generated field propagates in a specific direction, with a wave vector defined by the phase matching condition, and thus one can, in principle, collect the entire generated signal. Furthermore, the frequency resolution of these four-photon processes is limited only by the power-spectral-densities of the laser sources utilized, which are narrower than conventional spectrometer resolutions. At last, a further advantage of these techniques, especially when applied to microscopy, is the capability of three-dimensional sectioning, which is essential for imaging thick tissues or cellular structures.

After a theoretical introduction to non-linear interaction between light and matter, CARS and SRS will be widely discussed, and some of the main results currently achieved will be presented.

1.1 Nonlinear matter-light interaction

Every time an electric field interacts with a dielectric material, the molecules respond with a polarization *P*. This polarization vector can be expanded in series as:

$$P = P^{(1)} + P^{(2)} + P^{(3)} + \cdots \qquad (1.1)$$

where $P^{(i)}$ is the *i*-th order polarization. Each term of this series can be written as an electric field function:

$$P(E) \propto \varepsilon_0\left(\chi^{(1)}E + \chi^{(2)}E^2 + \chi^{(3)}E^3 + \cdots\right) \qquad (1.2)$$

$\chi^{(1)}$ is the linear electric susceptibility of the medium, $\chi^{(2)}$ is the second order susceptibility, $\chi^{(3)}$ is the third order susceptibility, and so on[1]. Every kind of medium has non-zero linear and third order susceptibilities, whereas only in non-centrosymmetric mediums the second order χ is different from zero. While the linear susceptibility rules the linear absorption, the third order one is responsible for many non-linear processes, the most visible one is decided by imposing particular conditions on the experiment as the *phase matching condition*.

The purpose of this paragraph is to explain what happens when light interacts with a material, more precisely which are the effects of the non-linear response of the material.

Using a semi-classical approach, starting from Maxwell's equations, and referring to a non-magnetic medium, without any charge or any current, under the hypothesis of plane waves, the following equation can be easily obtained:

$$\frac{\partial^2 E(z,t)}{\partial z^2} - \frac{1}{c^2}\frac{\partial^2 E(z,t)}{\partial t^2} = \mu_0 \frac{\partial^2 P(z,t)}{\partial t^2} \qquad (1.3)$$

The right side of the equation represents the response of the medium, and the polarization is the result of the contribution of a linear and a non-linear part. Adding the hypothesis of monochromatic wave, it's possible to express the field as:

$$E(z,t) = E_0 \cos(\omega_0 t - k_0 z) = E_0\, Re\left\{e^{i(\omega_0 t - k_0 z)}\right\} = E_0 e^{i(\omega_0 t - k_0 z)} \qquad (1.4)$$

For the next demonstrations the real part of the exponential function will be implicit.

Starting from equation (1.4) it is possible to derive the equation of a single pulse:

$$E(z,t) = A(z,t)e^{i(\omega_0 t - k_0 z + \varphi)} \qquad (1.5)$$

where A(z,t) is the expression of the envelope of the pulse, the exponential part is the carrier, and φ is the absolute phase between carrier and envelope.

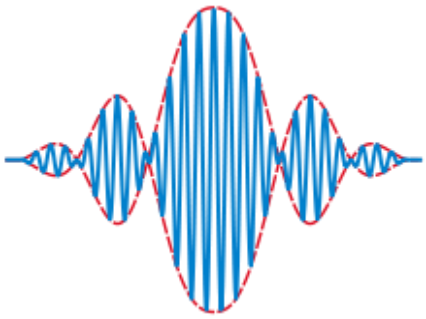

Fig.1.2 The red line represents the envelope, while the blue line shows the carrier

Applying the Fourier transform to equation (1.5) this expression is obtained:

$$\tilde{E}(z,\omega) = \tilde{A}(z,\omega - \omega_0)e^{-ik_0 z} \qquad (1.6)$$

The previous equation means that the pulse spectrum is exactly the envelope's one, shifted by ω_0. The polarization can be written as the sum of the two contributions:

$$P(z,t) = P_L(z,t) + P_{NL}(z,t) = \varepsilon_0 \chi^{(1)} E_0(z,t) e^{i(\omega_0 t - k_0 z)} + p_{NL}(z,t) e^{i(\omega_0 t - k_p z)} \qquad (1.7)$$

where p_{NL} is the envelope of the non-linear polarization and k_p is the carrier wave vector.

Generally $k_0 \neq k_p$ and this wave vector mismatch is usually indicated as $\Delta k = k_p - k_0$. Substituting (1.7) into (1.3) one obtains:

$$\frac{\partial^2 E(z,t)}{\partial z^2} - \frac{1}{c^2}\frac{\partial^2 E(z,t)}{\partial t^2} = \mu_0 \frac{\partial^2 P_L(z,t)}{\partial t^2} + \mu_0 \frac{\partial^2 P_{NL}(z,t)}{\partial t^2} \qquad (1.8)$$

Calculating the derivatives for the non-linear polarization:

$$\begin{cases} \dfrac{\partial P_{NL}(z,t)}{\partial t} = \left(\dfrac{\partial p_{NL}(z,t)}{\partial t} + i\omega_0 p_{NL}(z,t) \right) e^{i(\omega_0 t - k_p z)} \\ \dfrac{\partial^2 P_{NL}(z,t)}{\partial t^2} = \left(\dfrac{\partial^2 p_{NL}(z,t)}{\partial t^2} + i\omega_0 \dfrac{\partial p_{NL}(z,t)}{\partial t} + i\omega_0 \dfrac{\partial p_{NL}(z,t)}{\partial t} - \omega_0^2 p_{NL}(z,t) \right) e^{i(\omega_0 t - k_p z)} \end{cases} \qquad (1.9)$$

As a further hypothesis the derivatives of the amplitude term p_{NL} will be neglected.

According to (1.9), the equation (1.8) becomes:

$$\frac{\partial^2 E(z,t)}{\partial z^2} - \frac{1}{c^2}\frac{\partial^2 E(z,t)}{\partial t^2} = \mu_0 \frac{\partial^2 P_L(z,t)}{\partial t^2} - \mu_0 \omega_0^2 p_{NL}(z,t) e^{i(\omega_0 t - k_p z)} \qquad (1.10)$$

After applying the Fourier transform it becomes:

$$\frac{\partial^2 \tilde{E}(z,\omega)}{\partial z^2} - \frac{\omega^2}{c^2}\tilde{E}(z,\omega) = -\mu_0 \omega^2 \tilde{P}_L(z,\omega) - \mu_0 \omega_0^2 \tilde{p}_{NL}(z,\omega-\omega_0) e^{-ik_p z} \qquad (1.11)$$

where the expression of $\tilde{E}(z,\omega)$ is given in (1.6).

Calculating the derivatives of that term:

$$\begin{cases} \dfrac{\partial \tilde{E}(z,\omega)}{\partial z} = \left(\dfrac{\partial \tilde{A}(z,\omega-\omega_0)}{\partial z} - ik_0 \tilde{A}(z,\omega-\omega_0) \right) e^{-ik_0 z} \\ \dfrac{\partial^2 \tilde{E}(z,\omega)}{\partial z^2} = \left(\dfrac{\partial^2 \tilde{A}(z,\omega-\omega_0)}{\partial z^2} - 2ik_0 \dfrac{\partial \tilde{A}(z,\omega-\omega_0)}{\partial z} - k_0^2 \tilde{A}(z,\omega-\omega_0) \right) e^{-ik_0 z} \end{cases} \quad (1.12)$$

This time, because of the slowly variable envelope approximation, $\frac{\partial^2 \tilde{A}(z,\omega-\omega_0)}{\partial z^2}$ will be considered close to zero, and so neglected.

Substituting (1.12) into (1.11) and taking into account that in (1.7) one can express: $\chi^{(1)} = n^2(\omega) - 1$, after few mathematical calculations, one can easily obtain:

$$2ik_0 \frac{\partial \tilde{A}(z,\omega-\omega_0)}{\partial z} = [k^2(\omega) - k_0^2]\tilde{A}(z,\omega-\omega_0) + \mu_0 \omega_0^2 \tilde{p}_{NL}(z,\omega-\omega_0) e^{-i\Delta k z} \quad (1.13)$$

where $\Delta k = k_p - k_0$ is the wave vector mismatch and $k^2(\omega) = \frac{\omega^2 n^2}{c^2}$ is the generic wave vector at the angular frequency ω. For k values close one to each other this approximation is plausible:

$$k^2(\omega) - k_0^2 = (k(\omega) + k_0)(k(\omega) - k_0) \approx 2k_0(k(\omega) - k_0) \quad (1.14)$$

$k(\omega)$ can now be expanded in Taylor series as:

$$k(\omega) = k_0 + \frac{\partial k}{\partial \omega}\Big|_{\omega_0}(\omega - \omega_0) + \frac{1}{2}\frac{\partial^2 k}{\partial \omega^2}\Big|_{\omega_0}(\omega - \omega_0)^2 + \cdots =$$

$$= k_0 + \frac{1}{v_g}(\omega - \omega_0) + \frac{1}{2}GVD(\omega - \omega_0)^2 + \cdots \qquad (1.15)$$

where v_g is the group velocity and GVD is the group velocity dispersion. Higher order terms will not be considered in this argument, and in general this hypothesis is reasonable for pulses not too short. Substituting (1.14) and (1.15) into (1.13) this equation is found:

$$\frac{\partial \tilde{A}(z, \omega - \omega_0)}{\partial z} =$$

$$= -i\frac{1}{v_g}(\omega - \omega_0)\tilde{A}(z, \omega - \omega_0) - \frac{i}{2}GVD(\omega - \omega_0)^2\tilde{A}(z, \omega - \omega_0)$$

$$- i\frac{\mu_0 \omega_0 c}{2n}\tilde{p}_{NL}(z, \omega - \omega_0)e^{-i\Delta k z} \qquad (1.16)$$

It's now appropriate to come back again in the time domain applying the Fourier anti-transform:

$$\frac{\partial A(z,t)}{\partial z} = -\frac{1}{v_g}\frac{\partial A(z,t)}{\partial t} + \frac{i}{2}GVD\frac{\partial^2 A(z,t)}{\partial t^2} - i\frac{\mu_0 \omega_0 c}{2n}p_{NL}(z,t)e^{-i\Delta k z} \qquad (1.17)$$

The first two terms on the right side of the equation express the linear interaction between the pulse and the matter. The first one is the effect of the propagation and the second one of the dispersion in the material. If $GVD \neq 0$, then the pulse, during the propagation, will broaden in time, decreasing its peak power. If $GVD = 0$, then the pulse will travel unaffected by the medium. The third term on the right side of equation (1.17) takes into

account the effect of the non-linear response of the material. For a further simplification, we assume to consider a centro-symmetric material (i.e. $\chi^{(2)} = 0$).

According to equation (1.2) the nonlinear polarization can be expressed as:

$$P(t) \propto \varepsilon_0 \chi^{(3)} E^3(t) \qquad (1.18)$$

The incident electric field can be expressed as a sum of different fields, each of them generally corresponding to a different pulse. When considering third order effects, the incident field is the result of the superposition of three different pulses and his expression could be:

$$E(z,t) = \frac{1}{2}\left(A_1(z,t)e^{i(\omega_1 t - k_1 z)} + A_2(z,t)e^{i(\omega_2 t - k_2 z)} + A_3(z,t)e^{i(\omega_3 t - k_3 z)} + c.c.\right)$$

(1.19)

When (1.19) is put into (1.18) a vast number of terms arises from the cube of the electric field. In the following only the terms that are pertinent to the CARS and SRS effects will be considered; a more detailed discussion about all possible effects arising from the complete expansion of the non-linear polarization term is reported in Appendix A. From a physical point of view it has to be noted that the effect that actually takes place is always the one for which the phase matching condition is satisfied. Acting on the phase matching condition, it's in fact possible to select the desired effect.

Since both CARS and SRS can be regarded as a four wave mixing processes, let's now consider the so called *four wave mixing* process: three pulses focalized into a sample with frequencies ω_1, ω_2, and ω_3 mix together to merge into a different pulse with a different frequency $\omega_4 = \pm\omega_1 \pm \omega_2 \pm \omega_3$. As an example the combination $\omega_4 = \omega_1 + \omega_2 - \omega_3$ will be considered (it has to be $\omega_1 + \omega_2 > \omega_3$).

Knowing from equation (1.7) that $P_{NL}(z,t) = p_{NL}(z,t)e^{i(\omega_0 t - k_p z)}$, the following expressions can be obtained:

$$\begin{cases} P_{NL}^{\omega_1}(z,t) = 3\varepsilon_0 \dfrac{\chi^{(3)} A_2^*(z,t) A_3(z,t) A_4(z,t)}{8} e^{i[(-\omega_2+\omega_3+\omega_4)t-(-k_2+k_3+k_4)z]} \\ P_{NL}^{\omega_2}(z,t) = 3\varepsilon_0 \dfrac{\chi^{(3)} A_1^*(z,t) A_3(z,t) A_4(z,t)}{8} e^{i[(-\omega_1+\omega_3+\omega_4)t-(-k_1+k_3+k_4)z]} \\ P_{NL}^{\omega_3}(z,t) = 3\varepsilon_0 \dfrac{\chi^{(3)} A_1(z,t) A_2(z,t) A_4^*(z,t)}{8} e^{i[(\omega_1+\omega_2-\omega_4)t-(k_1+k_2-k_4)z]} \\ P_{NL}^{\omega_4}(z,t) = 3\varepsilon_0 \dfrac{\chi^{(3)} A_1(z,t) A_2(z,t) A_3^*(z,t)}{8} e^{i[(\omega_1+\omega_2-\omega_3)t-(k_1+k_2-k_3)z]} \end{cases} \quad (1.20)$$

Subsequently the wave vectors corresponding to the different frequencies will be considered as shown below:

$$\begin{cases} k_{p_1} = -k_2 + k_3 + k_4 \\ k_{p_2} = -k_1 + k_3 + k_4 \\ k_{p_3} = k_1 + k_2 - k_4 \\ k_{p_4} = k_1 + k_2 - k_3 \end{cases} \quad (1.21)$$

Before substituting (1.20) into (1.17) it is opportune to introduce one more hypothesis: $GVD \to 0$, because the difference between the group velocities of the pulses is more significant in a relatively small distance of interaction.

$$\begin{cases} \dfrac{\partial A_1(z,t)}{\partial z} + \dfrac{1}{v_{g_1}} \dfrac{\partial A_1(z,t)}{\partial t} = -i\alpha_1 \chi^{(3)} A_2^*(z,t) A_3(z,t) A_4(z,t) e^{-i\Delta kz} \\ \dfrac{\partial A_2(z,t)}{\partial z} + \dfrac{1}{v_{g_2}} \dfrac{\partial A_2(z,t)}{\partial t} = -i\alpha_2 \chi^{(3)} A_1^*(z,t) A_3(z,t) A_4(z,t) e^{-i\Delta kz} \\ \dfrac{\partial A_3(z,t)}{\partial z} + \dfrac{1}{v_{g_3}} \dfrac{\partial A_3(z,t)}{\partial t} = -i\alpha_3 \chi^{(3)} A_1(z,t) A_2(z,t) A_4^*(z,t) e^{i\Delta kz} \\ \dfrac{\partial A_4(z,t)}{\partial z} + \dfrac{1}{v_{g_4}} \dfrac{\partial A_4(z,t)}{\partial t} = -i\alpha_4 \chi^{(3)} A_1(z,t) A_2(z,t) A_3^*(z,t) e^{i\Delta kz} \end{cases} \quad (1.22)$$

In equations (1.22) $\alpha_i = \frac{3\omega_i}{8 n_i c}$ and $\Delta k = k_4 + k_3 - k_1 - k_2$.

These are a set of coupled equation that can be solved only with numerical methods, or introducing some simplifications. Solving one of them is possible to understand what happens to the corresponding frequency pulse. In the next paragraphs they will be solved under appropriate conditions, to show CARS and SRS signals that one expect to experience during these kind of experiments.

1.2 Coherent Anti-stokes Raman Scattering (CARS)

In the most commonly adopted configurations, CARS is a four wave mixing process driven by two fields that interact on the sample together at the same time in the same focal spot. Two pump photons at the frequency ω_p and a Stokes photon at the frequency ω_S interact and, satisfying the right phase matching condition, a four wave mixing process takes place.

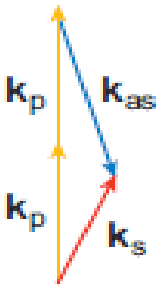

Fig.1.4 Phase matching condition for a CARS process[4]

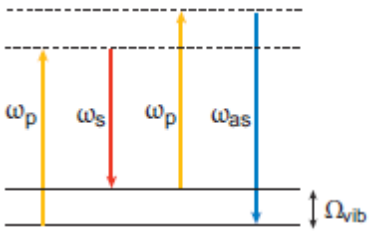

Fig.1.3 Energy-level diagram for the CARS technique[4]

The purpose of this paragraph is to obtain, starting from the generic equation derived from Maxwell equations, an analytical expression of the CARS signal. Taking into account equations (1.22) and imposing for the pump: $\omega_1 = \omega_2 = \omega_p$ and for the Stokes: $\omega_3 = \omega_S$, for the outgoing beam is then automatically obtained: $\omega_4 = 2\omega_p - \omega_S$ (Fig.1.3). When the frequency difference $\omega_p - \omega_S$ matches the frequency of the vibrational transition Ω_{vib}, the resonance gives a higher resonant signal and the emitted photon is an anti-Stokes one.

To maximize this process one has to satisfy the phase match condition reported in Fig.1.4: $k_{AS} = 2k_p - k_S$[5].

It is now possible to rewrite (1.22) as:

$$\begin{cases} \frac{\partial A_p(z,t)}{\partial z} + \frac{1}{v_{g_p}} \frac{\partial A_p(z,t)}{\partial t} = -i\alpha_p \chi^{(3)} A_p^*(z,t) A_S(z,t) A_{AS}(z,t) e^{-i\Delta kz} \\ \frac{\partial A_p(z,t)}{\partial z} + \frac{1}{v_{g_p}} \frac{\partial A_p(z,t)}{\partial t} = -i\alpha_p \chi^{(3)} A_p^*(z,t) A_S(z,t) A_{AS}(z,t) e^{-i\Delta kz} \\ \frac{\partial A_S(z,t)}{\partial z} + \frac{1}{v_{g_S}} \frac{\partial A_S(z,t)}{\partial t} = -i\alpha_S \chi^{(3)} A_p^2(z,t) A_{AS}^*(z,t) e^{i\Delta kz} \\ \frac{\partial A_{AS}(z,t)}{\partial z} + \frac{1}{v_{g_{AS}}} \frac{\partial A_{AS}(z,t)}{\partial t} = -i\alpha_{AS} \chi^{(3)} A_p^2(z,t) A_S^*(z,t) e^{i\Delta kz} \end{cases} \quad (1.23)$$

$$\Delta k = k_{AS} + k_S - 2k_p \qquad (1.24)$$

The first two equations (1.23) for the pump pulses are identical, the third one is related to the Stokes pulse, and for CARS the most interesting is the fourth one, because it shows the behavior of the anti-Stokes beam. To solve it the easiest way is to assume to be in the frame of reference of the pulse with ω_{AS}, and to suppose that the phase velocity mismatch is not that relevant to be taken into account. This way the second term on the left side of each equation (1.23) can be neglected, and the system turns into:

$$\begin{cases} \frac{\partial A_p(z,t)}{\partial z} = -i\alpha_p \chi^{(3)} A_p^*(z,t) A_S(z,t) A_{AS}(z,t) e^{-i\Delta kz} \\ \frac{\partial A_S(z,t)}{\partial z} = -i\alpha_S \chi^{(3)} A_p^2(z,t) A_{AS}^*(z,t) e^{i\Delta kz} \\ \frac{\partial A_{AS}(z,t)}{\partial z} = -i\alpha_{AS} \chi^{(3)} A_p^2(z,t) A_S^*(z,t) e^{i\Delta kz} \end{cases} \quad (1.25)$$

The phenomenon upon which CARS is based is a rather strong one, nevertheless it's possible to assume that the pump and the Stokes pulses remain unchanged after the interaction, so it's possible to hypothesize that their intensities are unaffected by this process: $A_p(z,t) = A_p \simeq const$, $A_S(z,t) = A_S \simeq const$. Therefore the last equation of (1.25) can be analytically resolved for an interaction length L:

$$\int_0^L dA_{AS}(z,t) = -i\alpha_{AS}\chi^{(3)}A_p^2A_S^* \int_0^L e^{i\Delta kz}\, dz \qquad (1.26)$$

After few processing and imposing $A_{AS}(0,t) = 0$:

$$A_{AS}(L,t) = -i\alpha_{AS}\chi^{(3)}A_p^2A_S^* L e^{\frac{i\Delta kL}{2}} \operatorname{sinc}\frac{\Delta kL}{2} \qquad (1.27)$$

The photodetector is intensity-sensitive, so from (1.27) it is useful to obtain the expression for the intensity of the Anti-Stokes beam:

$$I_{AS}(L,t) \propto |A_{AS}(L,t)|^2 \propto {\alpha_{AS}}^2 \left|\chi^{(3)}\right|^2 I_p^2 I_S L^2 \operatorname{sinc}^2\frac{\Delta kL}{2} \qquad (1.28)$$

The previous equation shows how the CARS signal is directly proportional to the Stokes intensity and proportional to the square of the pump intensity[4].

Condition (1.24) expresses the phase mismatch Δk and term $\operatorname{sinc}^2\frac{\Delta kL}{2}$ in equation (1.28) shows how the phase matching affects the signal. In a perfect phase matching condition ($\Delta k = 0$) that term becomes equal to 1, and then it is not to be taken into account. For non-

zero values of Δk the sinc function becomes smaller than 1 and the signal decreases in intensity.

One of the main differences between CARS and linear Raman spectroscopy is that here the measured intensity depends upon $\left|\chi^{(3)}\right|^2$ whereas the linear one depends simply on $\chi^{(3)}$. $\chi^{(3)}$ is linearly dependent on the density of oscillators, therefore CARS signal is proportional to the square of the density of vibrational oscillators.

$\chi^{(3)}$can be expressed as a sum of two terms, one resonant and one non-resonant:

$$\chi^{(3)} = \chi_{NR}^{(3)} + \chi_{R}^{(3)} = \chi_{NR}^{(3)} + \frac{N\sigma_R}{\Delta - i\Gamma} \qquad (1.29)$$

where $\Delta = \omega_p - \omega_S - \Omega_R$ is the detuning, Ω_R is the center of the Raman shift with a homogenously broadened line with bandwidth Γ, N is the number of molecules per unit of volume of the material, and σ_R is the Raman cross section[1] [4]. It is important to note that the non-resonant part of the susceptibility is purely real, while the resonant contribution has a real and an imaginary part.

Equation (1.29) shows that $\chi^{(3)}$ has different contributions. As seen before the phenomenon that occurs in CARS can be maximized by tuning the frequency difference between the two beams ($\omega_p - \omega_S$) to correspond to the vibrational transition to be probed. In this case $\Delta = 0$ and the resonant part of the $\chi^{(3)}$ is maximized and predominate.

Even when this difference is tuned far away from vibrational resonances, however, the pump and the Stokes fields can induce a polarization at the anti-Stokes frequency due to the electronic response of the material. In this condition, this polarization leads to a vibrationally non-resonant contribution to the CARS signal.

Since CARS intensity is proportional to $\left|\chi^{(3)}\right|^2$, it is possible to show this dependance:

$$I_{AS}(\Delta) \propto \left|\chi_{NR}^{(3)}\right|^2 + \left|\chi_R^{(3)}(\Delta)\right|^2 + 2\chi_{NR}^{(3)} Re\left\{\chi_R^{(3)}(\Delta)\right\} \qquad (1.30)$$

The first term is independent from the detuning and it's known as the non-resonant background. The second term contains only resonant information, and it is the dominant contribution when probing resonant scatterers. Mixing between the non-resonant and resonant contributions creates the third term, which contains the real part of the vibrational response.

In Fig.1.5 the black line represents the non-resonant background term, the blue line is the real part of the resonant term (χ' in the figure), and the red line shows the imaginary part of the resonant term (χ'' in the figure), the mixing between the non-resonant term and the resonant one is represented by the green line. The purple line plots the overall CARS signal, showing how it is complicated to read, due to a slight frequency shift and to the presence of sorts of plateaus, one positive and one negative on both sides of the curve[4].

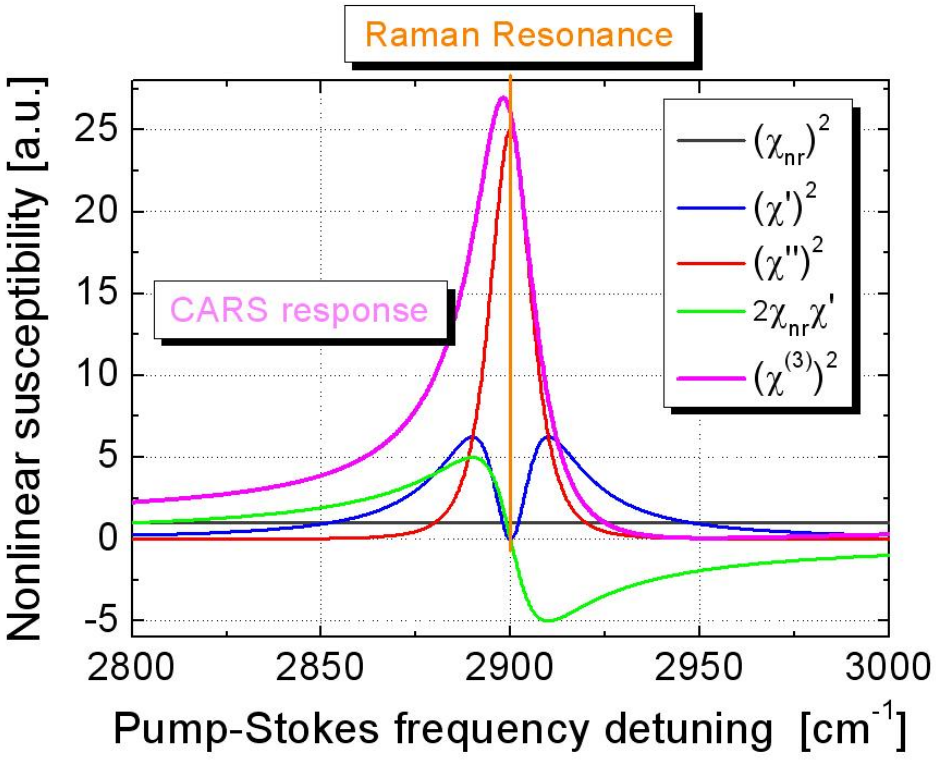

Fig.1.5 Different contributions to the CARS signal

1.3 Stimulated Raman Scattering (SRS)

The *stimulated Raman* effect was first observed in the early 1960s and since then it has been used in many spectroscopy studies. In SRS two laser beams, the pump with frequency ω_p and the Stokes with frequency ω_S, coincide on the matter. This phenomenon produces a gain in the Stokes beam when the frequency difference $\omega_p - \omega_S$ of the two fields is equivalent to a Raman frequency of excitation in the material. A Raman (SRG) gain is achieved when the probe frequency ω_S is less than the pump frequency ω_p. A Raman loss (SRL) is achieved when $\omega_S > \omega_p$. Fig.1.6 shows that this process can be seen as a degenerate four wave mixing process, thus it depends on the third order susceptibility of the probed medium. Unlike CARS, in SRS there is no emission at a different frequency, but only the two incoming beams are exchanging energy[2], as pointed out in Fig.1.7.

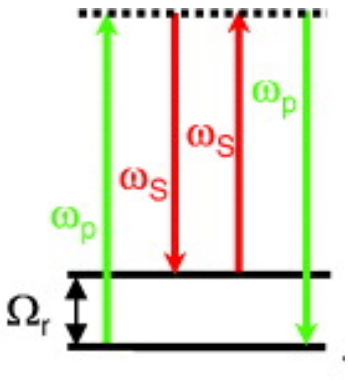

Fig.1.6 Energy levels involved in SRS process

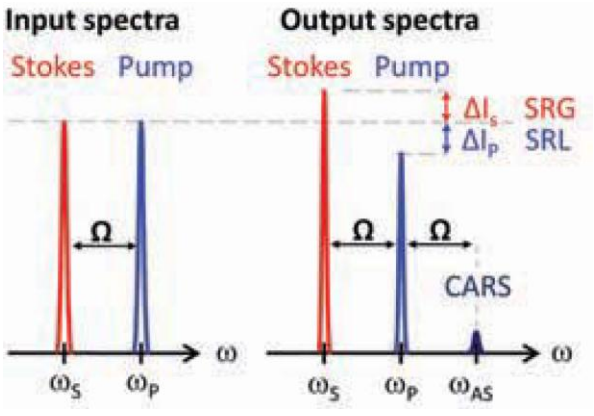

Fig.1.7 Input and output spectra for SRS and CARS processes[2]

In this paragraph the goal is to write an expression for the SRS signal, starting from equation (1.22), thus from Maxwell equations. This can be done by imposing the condition: $\omega_1 = \omega_3 = \omega_p$ for the pump and $\omega_2 = \omega_S$ for the Stokes beam. Automatically the frequency of the outgoing beam has to be $\omega_4 = \omega_p + \omega_S - \omega_p = \omega_S$. The set of equations (1.22) is hereby reduced to the two following equations:

$$\begin{cases} \dfrac{\partial A_p(z,t)}{\partial z} + \dfrac{1}{v_{g_p}} \dfrac{\partial A_p(z,t)}{\partial t} = -i\alpha_p \chi^{(3)} A_S^*(z,t) A_S(z,t) A_p(z,t) \\ \dfrac{\partial A_S(z,t)}{\partial z} + \dfrac{1}{v_{g_S}} \dfrac{\partial A_S(z,t)}{\partial t} = -i\alpha_S \chi^{(3)} A_p^*(z,t) A_p(z,t) A_S(z,t) \end{cases} \qquad (1.31)$$

Notice that in equations (1.31) there is no phase term. That's because $\Delta k = k_S + k_p - k_S - k_p = 0$ and so the phase matching is automatically achieved: this process always takes place. We are now interested in understanding what happens to the Stokes beam when it interacts with the strong pump field in a regime of negligible depletion, thus only the second equation is relevant.

Considering as usual the frame of reference of the Stokes beam, and considering a low pump depletion regime ($|A_p|^2 \simeq const$) equation (1.31) becomes:

$$\frac{\partial A_S(z,t)}{\partial z} = -i\alpha_S \chi^{(3)} |A_p|^2 A_S(z,t) \qquad (1.32)$$

This equation can be analytically solved:

$$\int_0^L dA_S(z,t) = -i\alpha_S \chi^{(3)} |A_p|^2 \int_0^L A_S(z,t)\, dz \qquad (1.33)$$

After few calculations it turns into:

$$A_S(L,t) = A_S(0,t)e^{-i\alpha_S\chi^{(3)}|A_p|^2 L} \qquad (1.34)$$

The exponential term in the previous equation can be expanded in a Taylor series to become:

$$A_S(L,t) = A_S(0,t)\left(1 - i\alpha_S\chi^{(3)}\left|A_p\right|^2 L\right) \qquad (1.35)$$

The expression needed is the one that gives the intensity for the Stokes beam, so the absolute square of equation (1.36):

$$I_S(L,t) \propto |A_S(L,t)|^2 \propto I_S(0,t)\left[1 + \left|i\alpha_S\chi^{(3)}I_p L\right|^2 - 2Re\{i\alpha_S\chi^{(3)}I_p L\}\right] \qquad (1.36)$$

In an SRS experiment the relative intensity variation is measured, which has a plus sign (gain) for the Stokes beam and a minus sign (loss) for the pump beam. For simplicity only the case of the SRG will be discussed, the SRL signal is equal to the SRG signal, but it can be calculating starting from equation (1.31) for the pump. The meaningful quantity we are looking for is therefore:

$$\frac{\Delta I_S(L,t)}{I_S(0,t)} = \frac{I_S(L,t) - I_S(0,t)}{I_S(0,t)} \qquad (1.37)$$

In equation (1.36) the term $\left|i\alpha_S\chi^{(3)}I_p L\right|^2$ can be neglected, so (1.37) becomes:

$$\frac{\Delta I_S(L,t)}{I_S(0,t)} = SRS = -2Re\{i\alpha_S\chi^{(3)}I_p L\} \qquad (1.38)$$

Calling back to mind equation (1.29) one can observe that $\chi^{(3)}$ has two contributions. The non-resonant part is real, the resonant one is complex. According to equation (1.38) only the real part of $i\alpha_S\chi^{(3)}I_pL$ has to be considered, which implies that the imaginary part only of $\chi^{(3)}$ contributes to SRS signal. This peculiar feature allows this technique to be free from the non-resonant background that affects the CARS signal. That means that in principle the reading of SRS measurements should be simpler compared to those coming from CARS data, being them distorted by a spurious contribution of the resonant and non-resonant part of the susceptibility.

From these considerations reported above one can write:

$$SRS \propto Im\{\chi^{(3)}\}I_pL \qquad (1.39)$$

Equation (1.39) shows that SRS signal does not depend on the Stokes intensity, but only on the pump one. It also linearly depends on the interaction length and on the imaginary part of the resonant $\chi^{(3)}$.

This is the most relevant difference between SRS and CARS: with SRS one has a direct access to the resonant response of the material, without any spurious contribution of the non-resonant background. Thus it is much simpler to interpretate the images coming from SRS, but on the other hand, the SRG/SRL signals are quite low (below 10^{-4}) requiring implementation of highly sensitive setups[2] [3].

The last limitation of CARS that can be overcame by SRS concerns the signal dependence on the concentration of the molecules. In the previous paragraph it was shown that CARS signal depends on the second power of the density of the oscillators, so it scales with a second power of *N*. SRS is linearly dependent on $\chi^{(3)}$, thus it is also linearly dependent on the density of oscillators *N*. This allows us to detect signals coming from a more diluted solution compared to those detectable out of the non-resonant background with CARS techniques (see Chapter 4 for results of dilution tests).

1.4 CRS state of the art

The most challenging goal when studying CRS techniques, is to obtain a sensitive, compact, versatile, and cost-effective system to perform optical microscopy. Nonetheless when switching from spectroscopy to microscopy many problems and critical aspects have to be taken into account. Now the stability, the sensitivity, the contrast, and the speed are crucial parameters indeed. In this paragraph some of the latest results published in the field of interest of this chapter will be briefly presented.

At first CARS imaging technique will be discussed. It is the most widely adopted technique so far, it can be applied not only to thin or weakly scattering samples, it has the capability for future use in clinical settings as an in situ imaging technique, and it provides imaging speeds up to the video-rate where narrowband pulses are used. After CARS, the recently exploited SRS will be presented

The first CARS microscope was built using a non-linear geometry, allowing the incoming beams to accomplish the vectorial relation shown in Fig.1.4. In 1999 a discovery cleared the way for modern CARS microscopy: near-infrared light focused by high NA objectives (NA>0.8) drives the $sinc^2$ function in equation (1.28) to asymptotically approach 1, rendering non-collinear geometries unnecessary[4]. Since then most of the experimental apparatus used are based on a collinear configuration. Other parameters, however, have to

satisfy some main requirements. A list of the main required parameters of the laser system for CARS microscopy can be found in Fig.1.8:

Parameter	Optimal Range
Pump wavelength range	780–980 nm
Stokes wavelength range	1000–1300 nm
Pulse duration	2–7 ps
Spectral bandwidth	3–5 cm^{-1}
Pulse energy	0.1–1 nJ
Pulse repetition rate	50–100 MHz

Fig.1.8 Parameters of laser light sources for CARS microscopy[4]

The first fundamental consideration regards the laser source choice. Sources in NIR minimize the non-resonant background generated by a nearby two-photon resonance. This two-photon absorption is generated by ultraviolet electronic transitions and causes, among others, the multiphoton absorption-induced photodamage. NIR light also allows pulses to penetrate more deeply in diffusive materials, with less intensity losses and focal spot size increasing. On the other hand, choosing a long wavelength means to accept a tradeoff with the spatial resolution; in fact, in these cases the detection is diffraction-limited, that means that to a longer wavelength corresponds a worse resolution, and vice versa.

Pulsed sources are required because the CARS effect depends on the intensities of the two incoming beams, but the choice of the pulse length is quite critical. From one point of view a femtosecond pulsed laser source grants enough intensity to experience high signals, but on the other hand a 100-fs-duration pulse is about 150 cm^{-1} in bandwidth, which is too high

to resolve a vibrational transition, whose linewidth tipically is 10-20 cm^{-1}. A femtosecond pulsed system centered on a resonance will, therefore, only use a small part of its spectral components to pump the narrow Raman line, but will generate a large non-resonant background signal, that can obscure or distort the resonant signal[4].

Initial CARS setups made use of two picosecond Ti:sapphire lasers synchronized by an electronic active control[12][13]. This complex and costly setup has been replaced by a more recent system composed by an optical parametric oscillator (OPO) pumped by a picosecond Nd:YVO_4 oscillator[11]. Such a system solves some problems (e.g. allows to probe a broader range of Raman shifts) but still has the main limitation in the fact that it has an insufficient flexibility since it does not allow to easily generate a third, tunable colour, that would be needed to perform more complex probing experiments. It has not been until recently that CARS setups based on a fiber laser have been developed. At first these system were working with broadband femtosecond excitation and spectral filtering of the emission. This method is highly spectrally inefficient, because the filtering cuts out most of the spectral power of the starting pulse. Another solution was to sum two oppositely chirped pulses, which is quite difficult. In this scenario, the spectral compression idea seemed to be the best one to combine the availability and flexibility of a femtosecond fiber source with the efficiency given by a narrowband pulse efficiently converted from a femtosecond one; it all with a rather simple setup, which is not too complicated to be operated in a non-specialist environment[10].

Independently from the used laser source, CARS microscopy suffers from being non-background free. In order to suppress the non-resonant background many solutions have been proposed and demonstrated. One of them exploits the fact that this non-resonant background does not depend on the frequency detuning and thus consists in detecting the resonant signal, which depends on both resonant and non-resonant terms of the susceptibility, and the signal out of resonance, and subtracting them to obtain only the resonant response.

Two different approaches have been proved: frequency modulation CARS (FM CARS) and differential two-signal picosecond CARS (DTSP CARS). The first one uses three different pulses: a small portion of a Nd:YVO_4 oscillator is used as a Stokes beam, while the other is used to synchronously pump an OPO and its output is used as a first pump, and a Ti:sapphire oscillator gives the second pump beam. The two pump beams are orthogonally polarized and a Pockels cell, driven by a square modulation waveform at 500 kHz, selects alternatively one of them. The lock-in thus reads a complete signal and the non-resonant background alternatively, and by selecting the right combination of wavelengths and powers the non-resonant term can be efficiently suppressed. FM CARS is most advantageous when the resonant signal is comparable with or smaller than the non-resonant background[16].

DTSP CARS uses only two beams, given by a Nd:vanadate laser, one directly used as the Stokes, the other one to synchronously pump an OPO. Instead of a dual-beam scheme using the signal and idler beams of the OPO, only the signal beam, which contains two

longitudinal modes with different wavelengths separated by only few nanometers, is used. The wavelength of one mode is adjusted at a peak, and the other mode at a background of the CARS spectrum. The dual-mode signal beam is spatially separated after the sample by using a grating spectrograph so that the background-suppressed image is instantaneously obtained from two CARS signal with a balanced detector. This technique, as well as FM CARS, showed an improvement in the contrast when used in imaging[15].

Another background-suppression technique is the heterodyne detection, also known as interferometric CARS (I-CARS). Such a technique uses the idea to superimpose the anti-Stokes signal with a coherent local oscillator. Many different setups have been used, based on different laser sources, but all of them exploit the idea that a coherent addition of a local field to the signal to be detected not only gives an amplification, which results in a less noisy measurement, but also allows one to detect, by setting the right phase to the local oscillator, the real mixing term or the imaginary resonant part of the susceptibility. This capabililty allows imaging with higher contrast, being based on a background-free reading[17][18][20]. Among all the similar solutions that have been proposed, one allowed to achieve a shot noise limited detection. The setup is based on a Nd:YAG laser: the main output is frequency doubled and the fundamental is used as a pump beam, while the second harmonic pumps an OPO. The idler of the OPO is used as a Stokes, while the signal is set to be the local oscillator. When this amplification scheme is combined to an Avalanche Photo Detector (APD), the shot noise limit is reached[19].

Many papers showed the capability of CARS to probe a specific vibrational resonance within a sample, and thus it is emerging as a powerful method for imaging biological and material specimens. However, the ability to acquire vibrational spectra over a significantly larger bandwidth would allow CARS to be used for identifying a large number of chemically distinct species and could be used to identify and track slight changes in complex systems. This is the case of broadband CARS or multiplex CARS (M-CARS). Works in this direction are concerned on implementing M-CARS with a one-laser setup, mainly a Ti:shappire. The output is spatially filtered in the Fourier plane to obtain a narrowband pump pulse, while the remainder is coupled in a non-linear fiber giving a continuum that spans over a wide range of wavelengths, thus allowing the setup to cover a broad range of Raman shifts (typically 400-4000 cm^{-1}). Several paper have demonstrated the feasibility of a broadband CARS microscopy, giving less spectral resolution, but more rejection to the non-resonant background compared to narrowband CARS[22][23][24].

SRS on the other hand, as previously shown in paragraph 1.3, automatically allows one to use a contrast mechanism which is background-free, because it probes the imaginary part of the susceptibility. Thus it does not need any particular background suppression technique. SRS appears in the form of a gain or a loss of the Stokes and pump beams, as first observed in 1962 and 1964[25]. Recently several papers were published demonstrating SRS as a contrast mechanism for imaging. Used setups, as for CARS, are different in terms of the chosen laser source to generate the two different wavelengths. The capability of this technique have been proved with two electronically synchronized Ti:shappire oscillators as well as with a Nd:YVO_4 pumping an OPO to obtain the tunable Stokes beam and directly

giving the pump beam. Both of them have been proved to be good solution for SRS microscopy once combined with high-frequency modulation and a lock-in amplifier, but it is only the second configuration that permitted to achieve a video-rate acquisition speed, which is a fundamental feature of this technique when applied to living samples[26].

CHAPTER 2

Raman-induced Kerr-effect spectroscopy

The so-called *RIKE* is another particular effect that takes place in materials when the third order polarization induces a significant non-linear response, known as *optical Kerr effect*.

The *optical Kerr effect* is a third order effect that occurs when a high intensity pump beam, with frequency ω_p, interacts with the matter. This beam may be thought of as inducing a complex anisotropic change in the refractive indices. As this happens, the axis parallel to the polarization of the pump beam, experiences a new value in its refractive index proportional to the beam intensity, while the orthogonal one does not change: the pulse inducts a birefringence. Such an optically-induced birefringence can be probed by making the sample interact with a second beam. This probe beam experiences the induced change in the refractive indeces, and its change in the polarization direction is detected. This measurement allows one to extract a signal which is proportional to the third order susceptibility.

As one could expect the detection scheme needed to achieve a polarization sensitive measurement is complicated indeed. In this Chapter, after presenting the physical phenomena that occur in this kind of spectroscopy and deriving the main equations that govern these processes, in the first two paragraphs, two main detection schemes usually adopted in these experiments will be presented: *crossed polarizers*, *OHD-detection*. After them, in the third paragraph the configuration adopted during this work will be presented: *balanced detection*.

First of all, in order to understand the phenomena which the medium undergoes during the interaction with two strong fields, let's suppose that in the same medium, while the pump induces the birefringence, another pulse hits the material, with frequency ω_S tuned in order to satisfy the resonance condition: $\omega_p - \omega_S = \Omega_{vib}$. In this case, if the Stokes beam has the same polarization of the pump beam, then an SRS effect takes place. If the Stokes beam has a different polarization, the anisotropy alters the polarization state of the Stokes beam. This change then can be detected by a polarization analyzer which is set to block the normal Stokes polarization

The two main configurations adopted in RIKES experiments differ in the polarization state of the pump beam, which can be linearly polarized at 45° (Linear RIKES) or circularly polarized (Circular RIKES), while the Stokes beam is horizontally or vertically polarized. To be more precise, not the absolute orientation of the polarization vectors in the frame of reference of the laboratory is significant, but the relative orientations of the two fields polarizations.

2.1 Crossed polarizers detection

2.1.1 Circular RIKES

In the following, let's assume that the pump beam is circularly polarized and the Stokes beam has only the horizontal component, as shown in Fig.2.1.

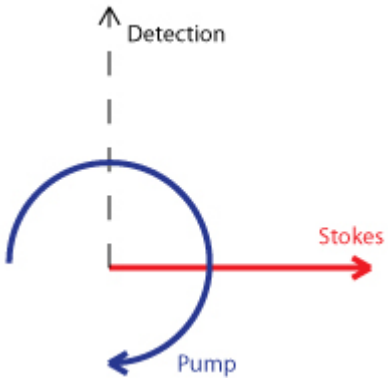

Fig.2.1 Polarizations scheme in circular RIKES with crossed polarizers detection

Thus the two fields may be written as:

$$\begin{cases} A_p = A_p^x + iA_p^y \\ A_S = A_S^x + A_S^y \end{cases} \quad (2.1)$$

where x and y indices are referred to the polarization components. For our discussion let's assume: $A_S^y = 0$ and $|A_p^x| = |A_p^y|$. In the first of equations (2.1) the complex field represents the circular polarization.

When using a circularly polarized pump, the effective $\chi^{(3)}$ can be shown to be written as:

$$\chi^{(3)} = i\left(\chi^{(3)}_{1212} - \chi^{(3)}_{1221}\right) \qquad (2.2)$$

where $\chi^{(3)}_{ijkl}$ is the susceptibility tensor element in which *i*, *j*, *k*, and *l* are the indices of the polarization components of the interacting electrical fields. Imposing: $A_1 = A_p^x, A_2 = A_S^x, A_3 = A_S^y,$ and $A_4 = A_p^y$, one may re-write the set of equations (1.22). For this argument only the equation for the y-component of the Stokes field is relevant, and thus considered.

Looking to equations (1.20), one can write the corresponding non-linear polarization term as:

$$P_{NL}^{\omega_S^y}(z,t) = 3\varepsilon_0 \frac{i\left(\chi^{(3)}_{1212} A_p^x(z,t) A_S^x(z,t) A_p^{y^*}(z,t) - \chi^{(3)}_{1221} A_p^y(z,t) A_S^x(z,t) A_p^{x^*}(z,t)\right)}{8} \quad (2.3)$$

It can be noted that the corresponding phase matching term vanishes, being the wave vectors the same as in SRS; therefore the phase matching condition is automatically achieved. Remembering that the two components of the pump field are equal, one can rewrite equation (2.3) as following:

$$P_{NL}^{\omega_S^y}(z,t) = \frac{3}{8} i\varepsilon_0\left(\chi^{(3)}_{1212} - \chi^{(3)}_{1221}\right) A_S^x(z,t)\left|A_p(z,t)\right|^2 \qquad (2.4)$$

Taking into account equations (1.22), the following equation is immediately obtained:

$$\frac{\partial A_S^y(z,t)}{\partial z} + \frac{1}{v_{g_3}} \frac{\partial A_S^y(z,t)}{\partial t} = \alpha_S\left(\chi^{(3)}_{1212} - \chi^{(3)}_{1221}\right) A_S^x(z,t)\left|A_p(z,t)\right|^2 \qquad (2.5)$$

Considering the frame of reference of the pulse, equation (2.5) can be written as:

$$\frac{\partial A_S^y(z,t)}{\partial z} = \alpha_S\left(\chi_{1212}^{(3)} - \chi_{1221}^{(3)}\right)A_S^x(z,t)\left|A_p(z,t)\right|^2 \qquad (2.6)$$

The previous equation can be easily solved:

$$\int_0^L dA_S^y(z,t) = \alpha_S\left(\chi_{1212}^{(3)} - \chi_{1221}^{(3)}\right)A_S^x(z,t)\left|A_p(z,t)\right|^2 \int_0^L dz \qquad (2.7)$$

Keeping in mind the initial condition: $A_S^y(0,t) = 0$, one obtains the linear expression for the new generated Stokes field with an orthogonal polarization (see Fig.2.1):

$$A_S^y(z,t) = \alpha_S\left(\chi_{1212}^{(3)} - \chi_{1221}^{(3)}\right)A_S^x(z,t)\left|A_p(z,t)\right|^2 L \qquad (2.8)$$

Calling back to mind equation (1.29) that shows the different contributions to the third-order susceptibility, one can remember that it is the sum of three different terms: a real non-resonant background, the real and the imaginary part of the resonant part. Being $\chi_{1212}^{NR} = \chi_{1221}^{NR}$, circular RIKES configuration cancels the non-resonant background.

Defining the effective susceptibility as: $\chi_{eff}^{(3)} = \chi_{1212}^{R} - \chi_{1221}^{R}$, and calculating the intensity corresponding to the detected RIKES signal, one obtains the following equation:

$$I_S^y(z,t) \propto \left|A_S^y(z,t)\right|^2 = {\alpha_S}^2\left|\chi_{eff}^{(3)}\right|^2 I_S^x(z,t){I_p}^2(z,t)L^2 \qquad (2.9)$$

Equation (2.9) shows that the RIKES signal is proportional to the intensity of the incoming Stokes beam, quadratically proportional to the intensity of the birefringence-inducing pump beam, and proportional to the absolute square of the effective susceptibility. The

simplest experimental way to detect this signal is to use two *crossed polarizers*. The first one, inserted before the sample in the Stokes path, is oriented in order to be sure to let only the horizontal polarization go in the sample. Another polarizer is put after the sample, rotated by 90°, in order to detect only the signal orthogonal to the incoming one. This way one is able to extract only the resonant contribution to the $\chi_{eff}^{(3)}$, but without the capability to discern the real part from the imaginary or vice versa.

2.1.2 Linear RIKES

When the pump beam, instead of being circularly polarized, is polarized at 45° degrees, as shown in Fig.2.2, the tensor element that can be probed is:

$$\chi^{(3)} = \left(\chi^{(3)}_{1212} + \chi^{(3)}_{1221}\right) \qquad (2.10)$$

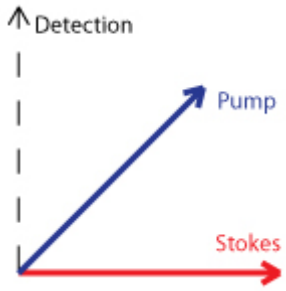

Fig.2.2 Polarizations scheme in linear RIKES with crossed polarizers detection

All the previous argument is still valid for this case, leading to write equation (2.8) as follows:

$$A_S^y(z,t) = -i\alpha_S\left(\chi^{(3)}_{1212} + \chi^{(3)}_{1221}\right)A_S^x(z,t)\left|A_p(z,t)\right|^2 L \qquad (2.11)$$

The main difference with the previous case is the absence of the rejection of the non-resonant background, making the signal more complicated to be read. The intensity of the linear-RIKES that can be detected is:

$$I_S^y(z,t) \propto \left|A_S^y(z,t)\right|^2 = {\alpha_S}^2\left|\chi^{(3)}_{eff}\right|^2 I_S^x(z,t){I_p}^2(z,t)L^2 \qquad (2.12)$$

where, this time, being $\chi_{eff}^{(3)}$ the sum of two different tensor elements with all the terms shown in equation (1.29), it gives rise to several spurious contributions that make this technique not background-free. Except for this term, linear RIKES shows the same dependences described above for the circular RIKES.

2.2 Optical Heterodyne-Detected RIKES

The main limitation in the *crossed polarizers* detection scheme is not to have the capability to get different signals that represent the real part or the imaginary one of the effective susceptibility; the only faculty that kind of system offers is to probe a superposition of real and imaginary parts. Furthermore, RIKES should theoretically be a background-free technique: one detects only the polarization component which is orthogonal to the one of the excitation beam. In practice, however, it is hard to suppress the excitation light sufficiently with the previous described detection scheme.[6]

Optical heterodyne detection (OHD) is a standard technique in spectroscopy. The general idea is that the small signal coming from the sample is amplified with a second, coherent electrical field A_{LO} at the same frequency, known as the local oscillator. In the following will be shown that this very technique allows one to overcome the limitation described above that is typical of the crossed polarizers technique.

Because of the coherent addition of the local field, the overall detected intensity is proportional to:

$$\left|A_{LO} + A_S^y\right|^2 = |A_{LO}|^2 + 2Re\{A_{LO}\}Re\{A_S^y\} + 2Im\{A_{LO}\}Im\{A_S^y\} + \left|A_S^y\right|^2 \qquad (2.13)$$

If $|A_{LO}|^2 \gg \left|A_S^y\right|^2$, the contribution of the last term in the previous equation is negligible compared to the mixing terms. If heterodyne detection is further combined with a modulation transfer scheme, the local oscillator term is suppressed, and equation (2.13) results in only the two remaining mixing terms.

Equation (2.13) can be therefore written as:

$$\left|A_{LO} + A_S^y\right|^2 \approx 2Re\{A_{LO}\}Re\{A_S^y\} + 2Im\{A_{LO}\}Im\{A_S^y\} \qquad (2.14)$$

Assuming to have an electronic controller able to set the phase of the local oscillator, it is now possible to set to zero either the real or the imaginary part of the local field. This way it is possible to detect the signal proportional to the real or the imaginary part of the outgoing probe beam.

2.2.1 Circular RIKES

As regards the circular RIKES, the equation giving the expression of the signal field to be amplified is (2.8). In Fig.2.3 is shown the polarization configuration of the beams involved in the process.

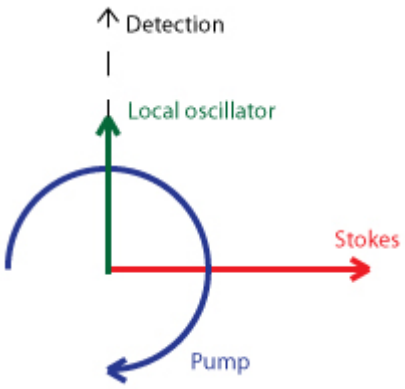

Fig.2.3 Polarizations scheme in circular OHD-RIKES

Thanks to the optical heterodyne detection we are able to look at the real or the imaginary part of the susceptibility setting the local oscillator phase as needed. Looking at equation (2.14) one can easily see that if A_{LO} is set to be $Im\{A_{LO}\} = 0$, then the expression of the detected intensity is the following:

$$I(z,t) \propto \left|A_{LO}(z,t) + A_S^y(z,t)\right|^2 \approx 2Re\{A_{LO}(z,t)\}Re\left\{A_S^y(z,t)\right\} \qquad (2.15)$$

Substituting equation (2.8) into (2.15), one obtains:

$$I(z,t) \propto 2\alpha_S Re\left\{\chi_{1212}^{(3)} - \chi_{1221}^{(3)}\right\} Re\left\{A_{LO}(z,t)A_S^x(z,t)\left|A_p(z,t)\right|^2\right\} L \qquad (2.16)$$

The previous equation shows that this technique allows one to measure the real part of the probed tensor elements. With this combination of parameters, looking at equation (2.16), one can realize that the two non-resonant components of the two tensor elements, being equal, are canceled. Thus this measurement is non-resonant background-free.

Differently, if A_{LO} is set to be $Re\{A_{LO}\} = 0$ then the expression of the detected intensity is the following:

$$I(z,t) \propto \left|A_{LO}(z,t) + A_S^y(z,t)\right|^2 \approx 2Im\{A_{LO}(z,t)\}Im\left\{A_S^y(z,t)\right\} \qquad (2.17)$$

Substituting equation (2.8) into (2.17), one obtains:

$$I(z,t) \propto 2\alpha_S Im\left\{\chi^{(3)}_{1212} - \chi^{(3)}_{1221}\right\} Im\left\{A_{LO}(z,t)A_S^x(z,t)\left|A_p(z,t)\right|^2\right\} L \qquad (2.18)$$

In this case one can obtain a measure of the difference between the imaginary parts of the two probed tensor elements, without any non-resonant background, being it caused by the real part of the susceptibility, as reported in equation (1.29). Looking at equation (2.9), which refers to circular RIKES detected with two crossed polarizers, one can immediately notice two advantages that OHD induces in the measurement: it allows to access directly to real or imaginary parts of the susceptibility and the detected signal intensity is proportional to the local field. This last key feature of the technique gives an important amplification of the signal to be detected, raising considerably the SNR.

2.2.2 Linear RIKES

Concerning the linear RIKES, equation (2.11) gives the expression of the probe field, after the interaction in the material. Fig.2.4 shows the configuration of polarizations of the three involved beams.

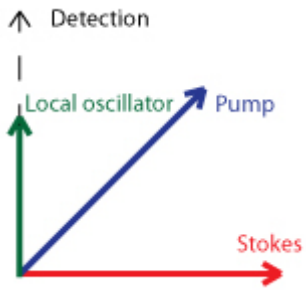

Fig.2.4 Polarizations scheme in linear OHD-RIKES

After mixing with the local oscillator, if A_{LO} is set to be $Im\{A_{LO}\} = 0$, then it is possible to write the detected intensity as:

$$I(z,t) \propto \left|A_{LO}(z,t) + A_S^y(z,t)\right|^2 \approx 2Re\{A_{LO}(z,t)\}Re\{A_S^y(z,t)\} \qquad (2.19)$$

Substituting (2.11) into (2.19) one can write:

$$I(z,t) \propto -2\alpha_S Re\left\{i\left(\chi_{1212}^{(3)} + \chi_{1221}^{(3)}\right)\right\} Re\left\{A_{LO}(z,t)A_S^x(z,t)\left|A_p(z,t)\right|^2\right\} L \qquad (2.20)$$

Keeping in mind the different contributions to the susceptibility reported in equation (1.29), one can easily realize that in this case is the resonant imaginary part of the sum of the two tensor elements to be probed, giving again a background-free measure.

Otherwise, if A_{LO} is set to be $Re\{A_{LO}\} = 0$, the detected intensity can be written as:

$$I(z,t) \propto \left|A_{LO}(z,t) + A_S^y(z,t)\right|^2 \approx 2Im\{A_{LO}(z,t)\}Im\{A_S^y(z,t)\} \qquad (2.21)$$

Substituting equation (2.11) into (2.21), one obtains:

$$I(z,t) \propto -2\alpha_S Im\left\{i\left(\chi_{1212}^{(3)} + \chi_{1221}^{(3)}\right)\right\} Im\left\{A_{LO}(z,t)A_S^x(z,t)\left|A_p(z,t)\right|^2\right\} L \qquad (2.22)$$

As in the previous case, it is immediate to understand that the first imaginary part term is nothing else than the sum of four contributions: the non-resonant parts of the two tensor elements and the real part of the resonant contributions. Therefore this case is the only one where the non-resonant background is not canceled.

	Circular RIKES	Linear RIKES
$Im\{A_{LO}\} = 0$	$Re\left\{\chi_{1212}^{(3)} - \chi_{1221}^{(3)}\right\}$	$Im\left\{\chi_{1212}^{(3)} + \chi_{1221}^{(3)}\right\}$
$Re\{A_{LO}\} = 0$	$Im\left\{\chi_{1212}^{(3)} - \chi_{1221}^{(3)}\right\}$	$Re\left\{\chi_{1212}^{(3)} + \chi_{1221}^{(3)}\right\}$

Fig.2.5 Dependence of the detected signal from the combinations of parameters in excitation light and phase of the local oscillator in OHD

Fig.2.5 shows all the combinations in the settings of polarization directions and phase of the local oscillator. Compared to the crossed polarizers detection scheme, OHD allows more flexibility; it permits, in fact, to obtain four different measurements. In this paragraph it has been shown that in three cases out of four the non-resonant background is suppressed, giving better results than with the simpler crossed-polarizers scheme, where in one case out of two the background is not suppressed. This advantage, added to an amplified signal leading to better SNRs, explains the reason to choose a more complicated setup to perform RIKES experiments.[6]

2.3 Balanced detection

The idea behind the work that led to this thesis was to find a different way to achieve a better sensitivity than in the crossed polarizers case, but without the setup complexity caused by the need of the local oscillator.

Optical heterodyne detection is a technique that allows one to have in three cases out of four a background-free measurement and, at the same time, gives an amplification of the signal, increasing remarkably the signal to noise ratio. OHD technique still has the main problem of being sensitive to the noise of the local oscillator. Nevertheless recent results show that this technique can be used to improve the sensitivity of the measurement system. On the other hand to perform an OHD experiment one has to accept an inevitable complication in the setup.

The balanced detection theoretically allows one to overcome the limitations pointed out in paragraph 2.1, and to do it with a rather simple setup. In addition, the detector used with this technique amplifies the difference between the optical powers detected by the two channels, giving a better noise rejection, being this to the first approximation canceled.

In order to perform a balanced detection experiment, first of all, one has to set up the measurement line in a way that both of the channels of the detector are balanced. To achieve this balancing one has to put a wave plate after the sample in such a way that the resulting beam is circularly or linearly at 45° polarized. With a Wollaston prism it is possible to separate the two components and send them to the detector. To have a better insight into the transformations that the probe beam undergoes after being modified by the birefringence in the sample, and to understand the combined effects of the wave plate and the Wollaston before the detector, the reader is invited to refer to Appendix B.

In this paragraph, starting from the results given by the argument developed in Appendix B, the following will show that with this technique the results obtained are similar to those got with OHD in terms of flexibility and capability to probe the real or the imaginary part of the susceptibility.

	Circular RIKES	Linear RIKES
λ/2 plate	$Re\left\{\chi_{1212}^{(3)\ R}\right\} - Re\left\{\chi_{1221}^{(3)\ R}\right\}$	$Im\left\{\chi_{1212}^{(3)}\right\} + Im\left\{\chi_{1221}^{(3)}\right\}$
λ/4 plate	$Im\left\{\chi_{1212}^{(3)}\right\} - Im\left\{\chi_{1221}^{(3)}\right\}$	$Re\left\{\chi_{1212}^{(3)\ R}\right\} + Re\left\{\chi_{1221}^{(3)\ R}\right\} + Re\left\{\chi_{1212}^{(3)\ NR}\right\} + Re\left\{\chi_{1221}^{(3)\ NR}\right\}$

Fig.2.6 Dependence of the detected signal from the combinations of parameters in excitation light and wave plates in balanced detection

Fig.2.6 shows that with the combination of circular and linear RIKES with two possible detection configurations is theoretically possible to retrieve from the signal the same information as for OHD (Fig.2.5) obtaining three out of four background-free measurements.

2.3.1 Circular RIKES

Let's consider first of all the circular RIKES. To obtain a circularly polarized pump beam, a λ/4 plate is inserted in the path with an angle of 45° between the optic axis of the wave plate and the vertical axis of the laboratory frame of reference.

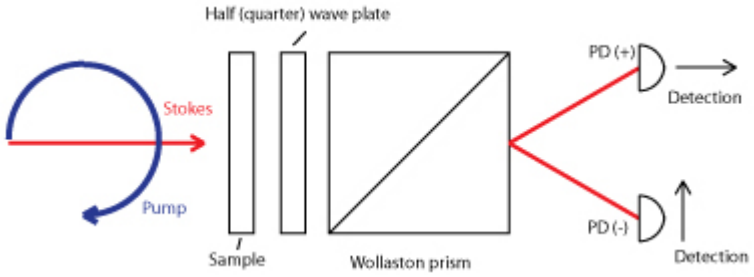

Fig.2.7 Polarization and detection directions in circular RIKES with balanced detection

In Fig.2.7 the configuration of excitation polarizations and detection direction is shown. With such a configuration one can probe the tensor elements:

$$\chi_{eff}^{(3)} = i\left(\chi_{1212}^{(3)} - \chi_{1221}^{(3)}\right) \qquad (2.23)$$

Being $\chi_{1212}^{(3)\ NR} = \chi_{1221}^{(3)\ NR}$, this tensor element has no non-resonant contributions, thus, in any of the two following cases, the resulting measurement is non-resonant background-free.

When a λ/2 plate is put after the sample, the detected signal has the expression given by equation (B.14):

$$\Delta I = 2Re\{A_S^x A_S^{y^*}\} \qquad (2.24)$$

Remembering equation (2.8), that gives us the expression of the Stokes field A_S^y after the light-matter interaction, one can re-write equation (2.24) as follows:

$$\Delta I = 2Re\left\{i\chi_{eff}^{(3)^*}\right\}\alpha_S I_S^x(z,t) I_p(z,t) L \qquad (2.25)$$

The most interesting part of equation (2.25) is the dependence from the real part of the effective $\chi^{(3)}$ multiplied by the imaginary unit. Looking at equations (2.23) and (2.25) one can easily notice that the imaginary unit is multiplied by itself, merging into a minus. Thus the real part of the $i\chi_{eff}^{(3)^*}$ is the difference of the two resonant real parts of the tensor elements represented by equation (2.23). This argument leads us to write the following:

$$|\Delta I| = 2\alpha_S\left(Re\left\{\chi_{1212}^{(3)^R}\right\} - Re\left\{\chi_{1221}^{(3)^R}\right\}\right) I_S^x(z,t) I_p(z,t) L \qquad (2.26)$$

The previous equation shows a linear dependence on the intensities of the Stokes and the pump beam. The detected signal can be small because the tensor element probed is a difference, and even if the two components of the susceptibility are not equal, they can be close one to each other. This measurement is background-free since there is no non-resonant term.

Differently, when a λ/4 plate is put after the sample, the detected signal has the following expression, given by equation (B.19):

$$\Delta I = 2Im\{A_S^x A_S^{y^*}\} \qquad (2.27)$$

The previous equation can be re-written, remembering equation (2.8) which gives the expression of the Stokes field A_S^y:

$$\Delta I = 2Im\left\{i\chi_{eff}^{(3)^*}\right\}\alpha_S I_S^x(z,t)I_p(z,t)L \qquad (2.28)$$

Being the effective susceptibility expressed by equation (2.23), when put into (2.28) gives rise to a minus. Thus the imaginary part of $\chi_{eff}^{(3)^*}$ is exactly the imaginary part to be taken into account in equation (2.28), leading to the following expression:

$$|\Delta I| = 2\alpha_S\left(Im\left\{\chi_{1212}^{(3)^R}\right\} - Im\left\{\chi_{1221}^{(3)^R}\right\}\right)I_S^x(z,t)I_p(z,t)L \qquad (2.29)$$

The previous equation shows that the detected signal depends linearly on the intensities of the Stoke and the pump beams and on the difference between the imaginary parts of the resonant contributions of the probed tensor elements. This signal can be quite low, due to dependence on the difference between the imaginary parts of the susceptibility, which can be similar, but it is still a background-free measurement, being equation (2.29) lacking in non-resonant terms.

2.3.2 Linear RIKES

To perform a linear RIKES experiment one has to put a λ/2 in the pump path with an angle of 22.5° between the optic axis of the wave plate and the vertical axis of the laboratory frame of reference. The configuration of the excitation polarizations and the detection directions is shown in Fig.2.8.

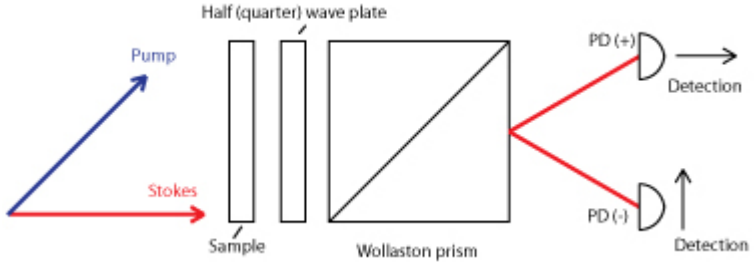

Fig.2.8 Polarization and detection directions in circular RIKES with balanced detection

In this experiment one can probe the tensor elements expressed by the following equation:

$$\chi_{eff}^{(3)} = \left(\chi_{1212}^{(3)} + \chi_{1221}^{(3)}\right) \qquad (2.30)$$

Again when a λ/2 is put after the sample, the corresponding measured signal is the one expressed by equation (B.14) or (2.24). Referring to equation (2.11) for the linear RIKES signal expression, one can put it into equation (2.24) to obtain the following:

$$\Delta I = 2Re\left\{i\chi_{eff}^{(3)\,*}\right\}\alpha_S I_S^x(z,t) I_p(z,t) L \qquad (2.31)$$

The previous equation is formally equal to equation (2.25), but it is different in the expression of the effective susceptibility, being it this time the one given by equation (2.30). Looking at these two equations, one can easily notice that the real part of $i\chi_{eff}^{(3)\,*}$ is proportional to the imaginary part of the effective susceptibility. The imaginary part is the sum of the two imaginary parts of the resonant contributions:

$$|\Delta I| = 2\alpha_S \left(Im\left\{ \chi_{1212}^{(3)\,R} \right\} + Im\left\{ \chi_{1221}^{(3)\,R} \right\} \right) I_S^x(z,t) I_p(z,t) L \qquad (2.32)$$

The previous equation shows that the differential signal detected is proportional to the intensity of the pump and the Stokes beams. It also allows one to notice that the signal is proportional to the sum of the sole imaginary parts, thus this measurement is background-free, being it caused by the real part of the effective $\chi^{(3)}$.

When a λ/4 plate is put after the sample the detected signal has the expression given by equations (B.19) or (2.27), and thanks to equation (2.11) one can write an equation equal to (2.28):

$$\Delta I = 2Im\left\{ i\chi_{eff}^{(3)\,*} \right\} \alpha_S I_S^x(z,t) I_p(z,t) L \qquad (2.33)$$

An argument similar to the one reported above for equation (2.31) leads us to consider that the imaginary part of $i\chi_{eff}^{(3)\,*}$ is actually the sum of the real parts of the tensor elements represented by equation (2.30). These elements are, as reported in equation (1.29), the sum of a non-resonant and a resonant contribution; the first one is real, while the second one is complex.

Thus the detected signal is:

$$|\Delta I| = \tag{2.34}$$

$$= 2\alpha_S \left(Re\left\{ {\chi^{(3)}_{1212}}^{R} \right\} + Re\left\{ {\chi^{(3)}_{1221}}^{R} \right\} + Re\left\{ {\chi^{(3)}_{1212}}^{NR} \right\} + Re\left\{ {\chi^{(3)}_{1221}}^{NR} \right\} \right) I_S^x(z,t) I_p(z,t) L$$

The previous equation shows, similarly to the previous cases, a linear dependence on the intensities of the pump and the Stokes beams. It also contains the real parts of the resonant terms of the tensor elements, but the measurement, in this case, is affected by the non-resonant background, expressed by: $Re\left\{ {\chi^{(3)}_{1212}}^{NR} \right\} + Re\left\{ {\chi^{(3)}_{1221}}^{NR} \right\}$.

2.4 RIKES state of the art

The RIKES effect has been demonstrated many decades ago, but since then it has not been widely exploited. As broadly explained in previous paragraphs, this technique should be background free, as the emission occurs with a different polarization from the one of the excitation light, which is usually stopped by the crossed polarizers. It is very hard, however, to suppress the excitation light sufficiently, and therefore it results in low sensitivities, ultimately giving a low resolution in microscopy applications.

Optical heterodyne is a well-known technique, but in other applications, e.g. CARS, had been performed with the local oscillator in the form of a third beam with the frequency to be detected in the excitation light, in order to measure real and imaginary parts of the susceptibility and suppress the non-linear background. In RIKES the emitted homodyne field from the sample has the same wavelength as the excitation field, but with a perpendicular polarization, thus allowing a background-free detection. If some of the excitation beam is rotated to match the emission polarization, it will provide a local oscillator with adjustable strength and phase.

It has been recently proved that it is possible to perform OHD-RIKES microscopy modifying the setup with a λ/2 plate used to slightly rotate the excitation light to control the power of the local oscillator and a compensator to continuously control the phase.

They found out that with such a technique, having some of the excitation light at the same detected frequency, one will observe at the same time SRS effect. Finding the best parameters to balance the heterodyne amplification with the unwanted SRS, they were able to acquire signals free from spurious background given by non-linear effects, achieving even higher sensitivity than in SRS. However, RIKES images showed a background given by the linear birefringence induced by the small fraction of the pump used as a local oscillator[6]. This background, in practice, is a serious obstacle in exploiting for microscopy purposes the potential sensitivity advantages of OHD-RIKES compared to SRS.

CHAPTER 3

Experimental setup

As explained in the first chapter, there are many requirements for the laser system that has to be used to perform CRS experiments. For standard applications two different narrowband, tunable, synchronized pulses are needed. In these spectroscopies in a first approximation the sensitivity depends on the bandwidth of the two pulses, the narrower the band, the highest the sensitivity achieved. To reach a bandwidth comparable to those typical of a vibrational transition, one has to use pulses durations down to few picoseconds. This chapter will allow the reader to know which was the setup used during the experiments.

The generation of tunable synchronized picosecond pulses is technically a non-trivial task. On the other hand, femtosecond sources are becoming more and more compact and reliable and allow easy tunability over broad spectral ranges, thanks to the non-linear effects that can be driven by such high-peak-power short pulses[9]. Our approach was to use a fiber femtosecond laser and to synthesize picosecond pulses.

3.1 Laser source

The laser system used in the experiments, shown in Fig.3.1, is based on a mode-locked Er:fiber oscillator (FemtoFiber pro, from Toptica Photonics).

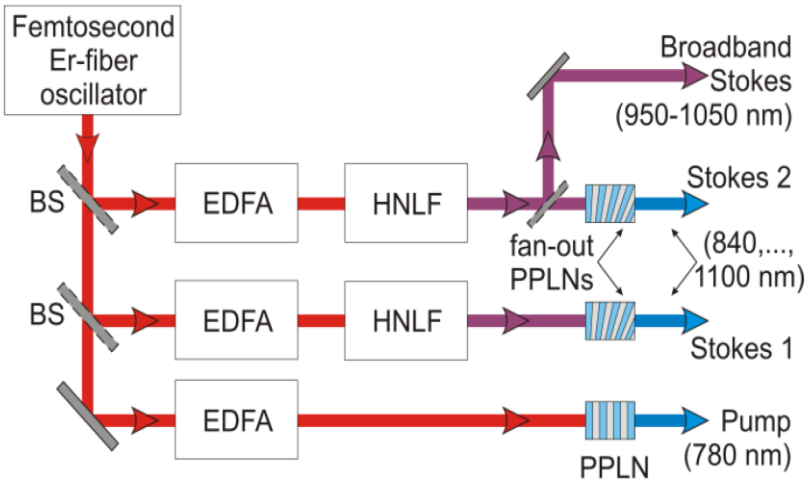

Fig.3.1 Architecture of the adopted laser system, driven by an Er:fiber oscillator. BS: beamsplitter; EDFA: Er-doped fiber amplifier; HNLF: highly non-linear fiber; PPLN: periodically-poled lithium niobate[9]

The oscillator has a linear cavity and semiconductor saturable absorber mirror, working at 40 MHz repetition rate. The output is used to feed three independent Er-doped fiber amplifiers (EDFAs), each producing 350 mW average power, corresponding to 9 nJ per pulse, at a 1560 nm central wavelength. All three EDFA outputs, which are synchronized and phase coherent, are compressed to nearly transform-limited sub-100-fs duration by a silicon prism pair. Two of the EDFA outputs are coupled to a highly non-linear fiber (HNLF) with a zero dispersion wavelength close to the input wavelength. Being the input

wavelength slightly higher than the zero dispersion one, it is laying in the anomalous dispersion regime. The pulses propagating in this regime undergo considerable spectral broadening, with the spectral energy density concentrating in two peaks on opposite sides of the input wavelength[9].

At longer wavelengths, were the dispersion is still anomalous (D<0), the pulse gives rise to a soliton. A soliton is a pulse which does not change its shape because of a delicate balance between dispersion and non-linear effects. Under particular conditions, these two effects are perfectly balanced and thus the pulse travels without changing its shape.

On the other side of the input wavelength, in the normal-dispersion regime (D>0), the soliton is accompanied by a dispersive wave. The exact positions of the peaks of soliton and dispersive wave depend on the overall dispersion of the input pulse, which can be controlled by acting on the silicon prism pair insertion. It results in the capability of the system to continuously tune the soliton peak between 1700 and 2100 nm, and to push the dispersive wave to wavelengths as short as 1000 nm[9].

Fig 3.2 shows the spectrum of the pump output (black line) and three examples of the long-wavelength part of the supercontinuum generated by HNLF (colored lines).

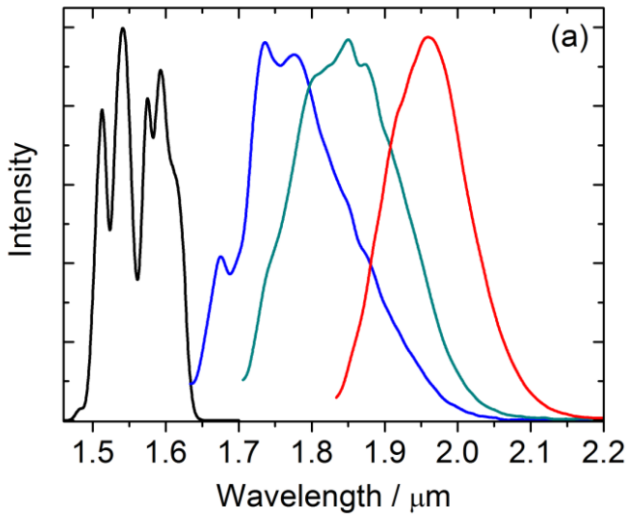

Fig.3.2 Spectrum of the main laser output at 1560 nm (black line) and examples of spectra of the long-wavelength part of the supercontinuum, tunable by acting on the input pulse chirp[9]

The processes described above easily generate tunable femtosecond pulses in the NIR region, but for CRS applications, longer narrowband picoseconds pulses are needed. Several linear and non-linear techniques are available to generate them starting from femtosecond pulses. Linear processes introduce high losses, whereas non-linear ones are often experimentally challenging. Since the goal of the work was to build a valuable and alternative setup compared to those traditionally used for spectro-microscopy purposes, it had to be also reliable and efficient.

3.2 Spectral compression of femtosecond pulses

Recent papers showed that a SHG process in a crystal with high group velocity mismatch between the fundamental ($v_{g_{FF}}$) and the second harmonic ($v_{g_{SH}}$) pulses can lead to an efficient generation of narrowband SH pulses starting from broadband FF ones.

Calling ω_0 the FF, one has to satisfy the following phase matching condition in order to achieve the maximum obtainable conversion efficiency:

$$\Delta k = k(\omega_0) + k(\omega_0) - k(2\omega_0) = 0 \qquad (3.1)$$

The FF is only a small portion of the spectral components found in the broadband pulse. In the broad spectrum of the femtosecond pulse there are several components with frequencies $\omega_0 \pm \Delta\omega$. While the SHG takes place, the SFG arises from these components, to give an output frequency $(\omega_0 + \Delta\omega) + (\omega_0 - \Delta\omega) = 2\omega_0$. The SFG's phase matching condition can be written as[14]:

$$\Delta k = \big(k(\omega_0 + \Delta\omega) + k(\omega_0 - \Delta\omega)\big) - k(2\omega_0) =$$

$$= k(\omega_0) + \left(\frac{\partial k}{\partial \omega}\right)_{FF} \Delta\omega + k(\omega_0) - \left(\frac{\partial k}{\partial \omega}\right)_{SH} \Delta\omega - k(2\omega_0) \qquad (3.2)$$

Keeping in mind the condition given by (3.1), equation (3.2) can be written as:

$$\Delta k = \left[\left(\frac{\partial k}{\partial \omega}\right)_{FF} - \left(\frac{\partial k}{\partial \omega}\right)_{SH}\right]\Delta\omega = \left(\frac{1}{v_{g_{FF}}} - \frac{1}{v_{g_{SH}}}\right)\Delta\omega \qquad (3.3)$$

It can be shown that the FWHM bandwidth of the SH pulse $\Delta\omega_{SH}$ is approximately:

$$\Delta\omega_{SH} = 0.866\frac{1}{|\delta|L} \qquad (3.4)$$

where L is the length of the crystal and $\delta = \frac{1}{v_{g_{FF}}} - \frac{1}{v_{g_{SH}}}$ is the temporal walk-off. Equation (3.4) shows that, with high group velocity mismatch and long crystals, the SH bandwidth can be quite narrow.

To achieve large spectral compression ratios and conversion efficiency as high as 40%, long crystals and large $|\delta|$ values are required. Periodically poled crystals seem to be the best choice thanks to their high non-linear coefficients and high δ values[9].

The described system uses two distinct MgO-doped periodically poled lithium niobate (PPLNs) crystals to generate the pump and the Stokes pulses. The 1560 nm output of the EDFA is compressed by a 10 mm long PPLN with a poling period of 19.3 μm and generates the pump pulses at a fixed 780 nm wavelength, with a 120 mW average power, and a 15 cm^{-1} of bandwidth. The soliton is frequency doubled with a 10 mm long PPLN crystal having a fan-out grating spanning the 22-33 μm range to produce Stokes pulses tunable from 840 to 1100 nm with power up to 10 mW[9].

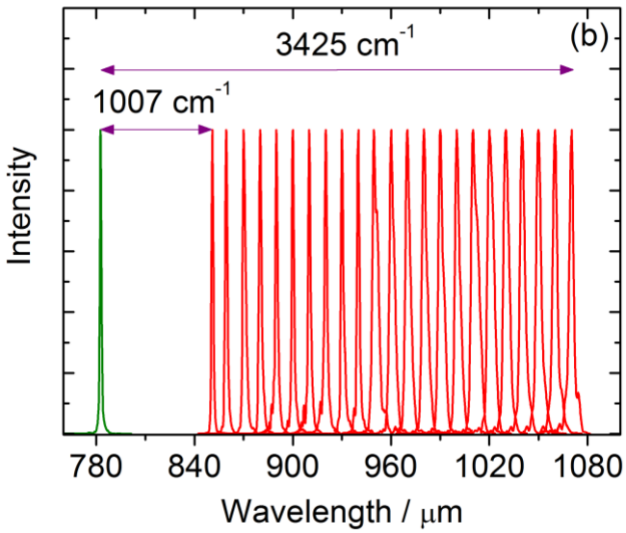

Fig.3.3 Spectra of the pump (green line) and the tunable Stokes pulse (red line), as obtained by spectral compression of the spectra reported in Fig.2.2[9]

In Fig.3.3 is shown that, by tuning the Stokes SH, it is possible to probe biologically relevant resonant frequencies in the samples in a wide range (1007-3425 cm^{-1}). Rapid tuning of the Stokes pulse is achieved by transversely translating the fan-out crystal. Translation was performed manually, but using a motorized stage could give automatic wavelength selection and reproducibility. The linewidth of the generated Stokes pulses ranges between 18 and 30 cm^{-1}, which is slightly higher than those achieved with different setups. It could be improved with a more carefully choice of the PPLNs parameters.

3.2 CARS and SRS setup

In Fig.3.4 is reported the setup used for CARS and SRS experiments. Pump and Stokes pulses are synchronized through a delay line mounted in the Stokes path, collinearly combined by a dichroic beam splitter (beam combiner), and focused by a microscope objective (60X, NA=0.7). The transmitted light is collimated by a long working distance objective (100X, NA=0.75). On the Stokes path a long-pass filter cuts out the wavelength below 800 nm, and for CARS detection a short-pass filter and a notch filter select the forward anti-Stokes signal, with a rejection of 10^{13} on the pump and Stokes beam, to be detected by a Si spectrometer. For SRS detection, the Stokes pulse, filtered from the pump through a long-pass and a notch filter, is sent to a balanced InGaAs photodiode (Nirvana 2017, from New Focus). The pump beam is acousto-optically modulated at a 70 kHz frequency, and a lock-in amplifier measures the SRG of the Stokes beam[9].

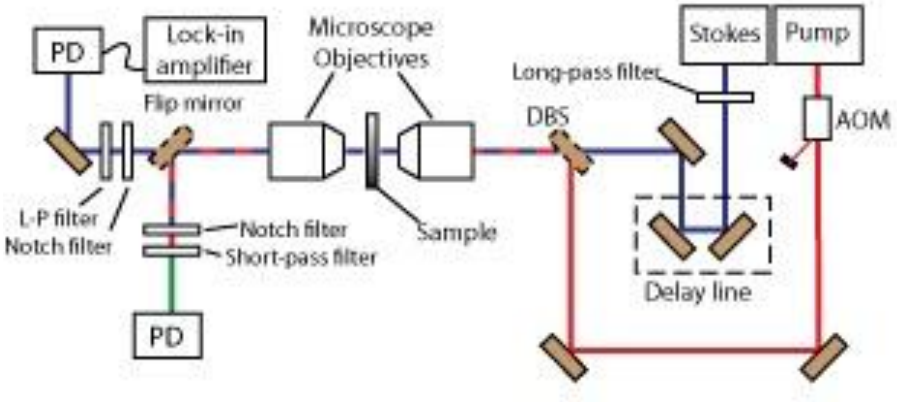

Fig.3.4 CARS and SRS setup. DBS: dichroic beam splitter; AOM: acousto-optic modulator; PD: photodetector

3.4 RIKES setup

Switching from CARS or SRS experiments to RIKES experiments is easy, thanks to a well-designed setup. In fact the only difference with the previously described setup is the addition of a half (or quarter) wave plate in the pump path, to linearly polarize at 45° (or circularly) the beam, and of a half (or quarter) wave plate after the sample. The effect of these last two wave plate is largely discussed in paragraph 2.3 and in Appendix B. A fraction of the Stokes beam is split off before the beam combiner and focused on the spectrometer to serve as a reference for the imaging software. In Fig.3.5 a sketch of the utilized setup is reported.

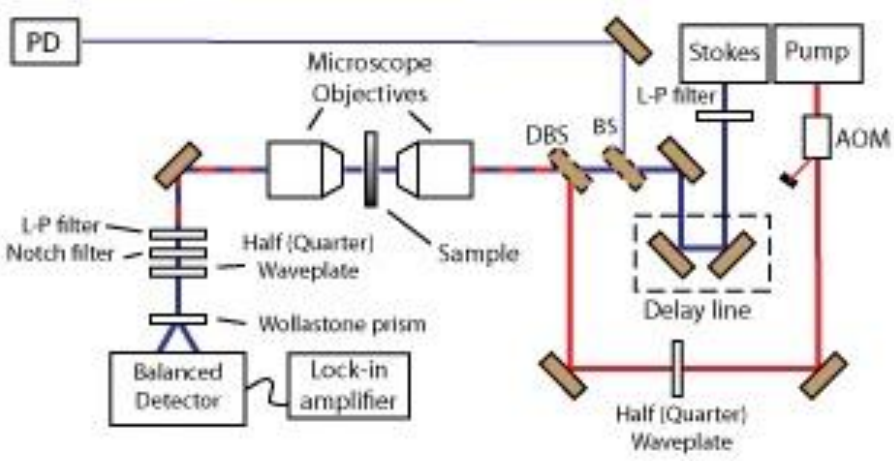

Fig.3.5 RIKES setup. AOM: acousto-optic modulator; BS: beam-splitter; DBS: dichroic beam-splitter; PD: photodetector

CHAPTER 4

Experimental results

The task of the experimental work of our group was to develop a brand new technological approach to CRS techniques, by designing a non-conventional setup for coherent Raman microscopy based on a compact fiber-format laser. To have a more detailed inner view of the experimental setup, it is preferable to refer to Chapter 3, where it has been discussed.

As preliminary tests while designing and building the setup, several spectra of the pump and the Stokes output were acquired. In Fig.3.2 and Fig.3.3 some of them are plotted, referring to the fundamental output without PPLN crystals and to the second harmonic output respectively. Since the performances of the laser were satisfying in terms of wavelength tunability, thus wide spectral coverage of vibrational transition that could be probed (1007-3425 cm^{-1}), and predicted spectral resolution (pulses bandwidth of 15-30 cm^{-1}), at first CARS and SRS experiments were run.

4.1 CARS and SRS spectroscopy

The spectra of several solvents were acquired in order to test the performances of the system, as shown in Fig.4.1. For each solvent it has been possible to tune the Stokes wavelength in order to find the correct detuning and to maximize the resonant signal by moving a screw from the outside of the laser, to span from 985 nm to 1045 nm of the Stokes wavelength, while the pump was fixed at 783 nm of wavelength. Plotted data reflect quite precisely the well-known spectra found in Raman bibliography.

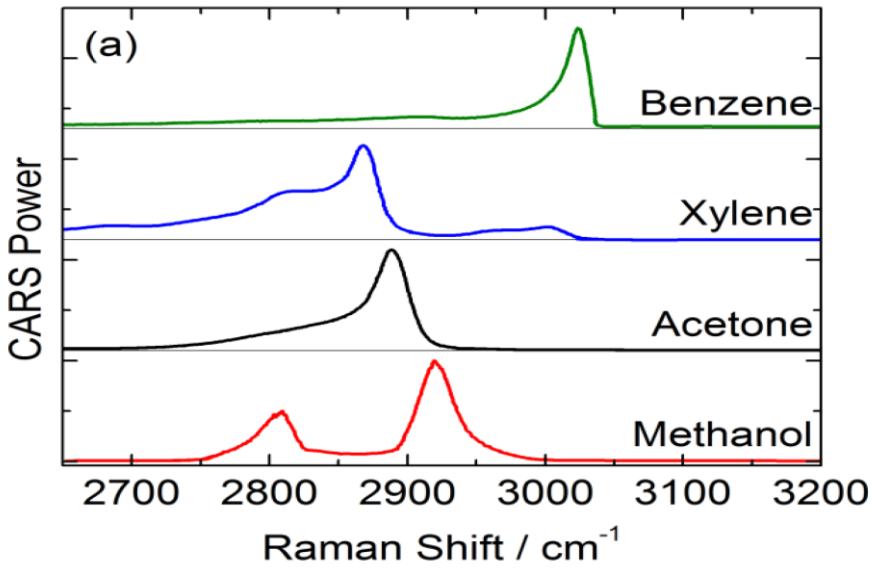

Fig.4.1 CARS spectra of different solvents

As expected CARS signatures are asymmetrically shaped, because of the non-resonant background contribution that creates a sort of plateau at wave numbers lower that the peak wave number. The system is currently limited to a spectral resolution of nearly 40 cm^{-1}, but

it could be improved with a more accurate design of the fan-out PPLN crystals of the laser. The CARS signal for methanol has shown a power in excess of 400 pW, 500 times higher than the one detected with the previously used setup.

Since the CARS results were satisfying, several SRS spectra were acquired to test the performances of the system with a more complicated experiment, and they showed a slightly broader response, due to the linear dependence compared to the quadratic one of the CARS signal on the non-linear susceptibility. Comparing Fig.4.1 and Fig.4.2 this difference is easily appreciable: as an example looking at the methanol spectra one can easily notice that there is a region between the two resonance peaks in SRS spectrum where the signal does not vanish. In Fig.4.2 it can also be observed that the SRS response shows a more symmetric behavior on the two sides on the resonance peak. These measurements were taken over an integration time of the lock-in amplifier of 300 ms.

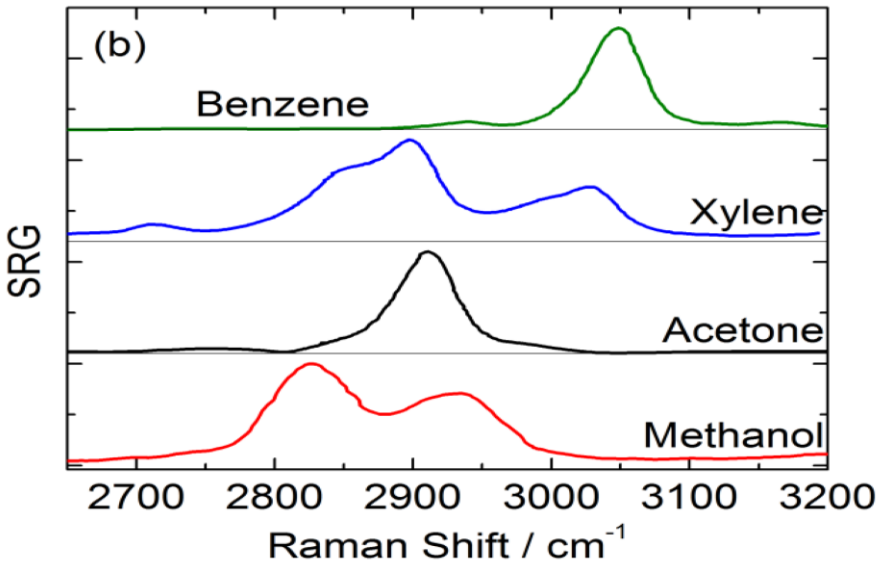

Fig.4.2 SRS spectra of different solvents

Our tests showed an SRG signal 10 times higher than those detected with the previous setup (e.g. in the order of 10^{-3} for the methanol). This improvement had to be paid with a worsening in the laser noise level, so that in the end the sensitivity over 500 ms of integration time has not hardly changed (from $2 \cdot 10^{-7}$ to $5 \cdot 10^{-7}$).

The last test run with CARS and SRS techniques was a dilution tests. In Chapter 1 it was demonstrated that CARS signal scales quadratically with the concentration of the oscillators, while the SRS signal linearly scales with the concentration. The goal was to verify this behavior by measuring CARS and SRS signals of a sample of acetone in water. At each step the concentration was halved by keeping half of the previous solution and filling the other half with water and the reading was made. Fig.4.3 shows the results of the dilution test, the square in the graph is a zoomed graph of the lower concentrations region.

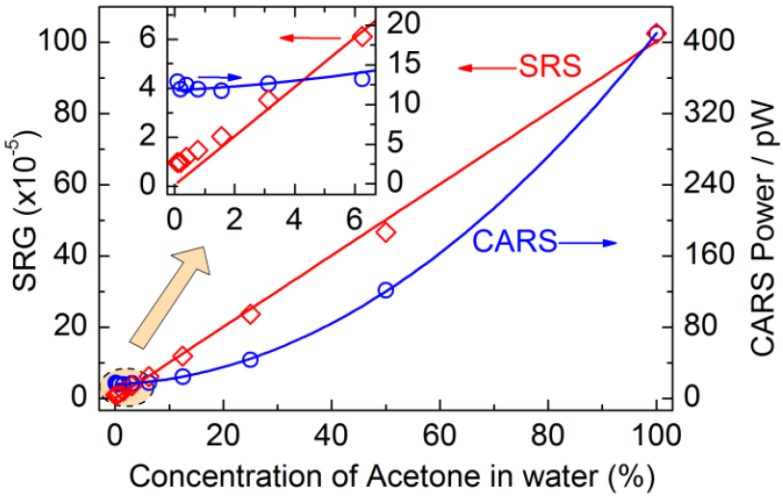

Fig.4.3 Dilution curves of acetone in water measured with CARS (blue circles) and SRS (red diamonds), together with quadratic and linear fitting curves, respectively. Inset shows a zoom for low acetone concentration

In Fig.4.3 the curves representing the linear and the quadratic dependence are plotted. With CARS technique one quickly reaches a constant value due to the strong non-resonant background contribution given from water, limiting the sensitivity to nearly 10% of volume concentration (corresponding to 1.4 M). Differently, the linear SRS response allows the detection of lower concentrations, down to nearly 0.5% (corresponding to 70 mM), being limited by the undesired resonant response of the water.

4.2 RIKES spectroscopy

After testing the system with preliminary CARS and SRS spectra acquisitions, acetone RIKES spectra where acquired in the four configurations explained in Chapter 2.3. Acetone, whose formula is $(CH_3)_2CO$, has the Raman spectrum reported in Fig.4.4. The transition to be probed was decided to be the highest one, with a resonance at nearly 2930 cm^{-1} in wavenumbers.

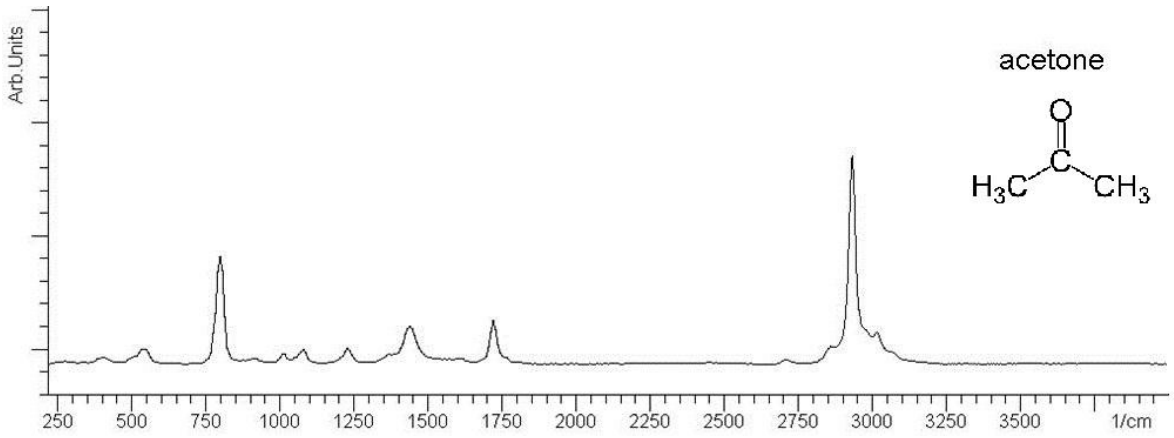

Fig.4.4 Raman spectrum of acetone and its chemical formula

By setting the correct combination of λ/2 and λ/4 plates for each acquisition, collecting a small portion of the Stokes beam as a reference, in order to normalize the collected data from the lock-in, RIKES spectra were collected by an *ad hoc* software recording the signal with the balanced detector. With an integration time of 300 ms the Stokes wavelength was manually and continuously scanned from 980 nm to 1040 nm.

These spectra are plotted in Fig.4.5, already normalized on the Stokes power.

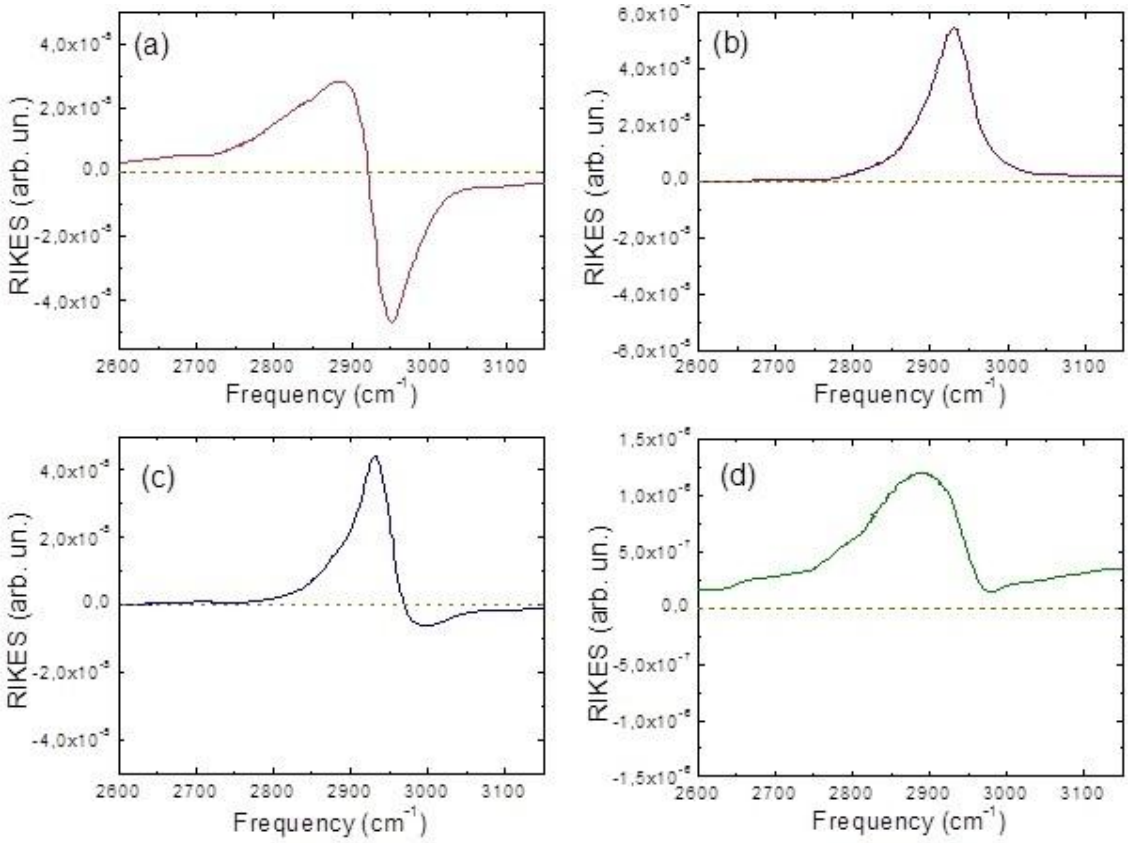

Fig.4.5 Acetone RIKES spectra with balanced detection in all the four configurations: (a) Circular-RIKES with λ/2 plate in detection (b) Linear-RIKES with λ/2 plate in detection (c) Circular-RIKES with λ/4 plate in detection (d) Linear-RIKES with λ/4 in detection

The previous spectra are reported reflecting Fig.2.2. Referring to that table one can note that spectrum (a) is the difference between two real parts, and thus it has a dispersive shape; it is the best spectrum representing real parts. Spectrum (b) is the sum of two imaginary parts and it seems to be the best one, both because it is a non-resonant background-free measurement and because to align λ/2 plates is much easier than to align λ/4 plates. Spectrum (c) is the difference between two imaginary parts and that is the reason why the signal goes below zero. In spectrum (d) we can recognize the effect of a

non-resonant background, added to an experimental difficulty in aligning the system with two λ/4 plates. These motivations lead the spectrum to have a not clear shape, and the peak to be slightly shifted towards smaller frequencies. Each of the other three spectra showed a resonance peak where it was expected to be found and spectral shapes similar to those expected.

4.3 SRS and RIKES microscopy

Once obtained previous spectra with CARS, SRS and RIKES technique, the setup was switched to microscopy configuration. The manual mechanical translator was replaced with a piezo-electric one connected to the pc through specific software to record images. Switching from SRS to RIKES microscopy consisted in setting up a linear-RIKES experiment with a λ/2 plate in the detection branch (see Paragraph 2.3). The choice was led by the best results obtained in RIKES spectroscopy experiments with this configuration and by the fact that this way, similarly to SRS, we are able to probe the sum of the imaginary parts of the tensor elements of the susceptibility (see Fig.2.2), thus the results are easier to be compared.

The experiment was run on a glass substrate with polystyrene (PS) and poly(methyl methacrylate) (PMMA) beads. SRS and RIKES images were acquired in the same spot in order to be able to compare them and to prove that RIKES in combination with the balanced detection gives less noisy signals and has the needed chemical specificity, being PS and PMMA CH stretching resonances at 3060 cm^{-1} and 2940 cm^{-1} respectively. Fig.4.6 (d) and (e) show PS beads acquired with SRS and RIKES respectively; comparing them is easily noticeable that SRS image is more blurry, and that is confirmed by the 2D profiles in Fig.4.6 (a) and (b). These signals are similar but the SRS one, while presents nearly the same spatial resolution as the RIKES profile, has a worse signal to noise ratio.

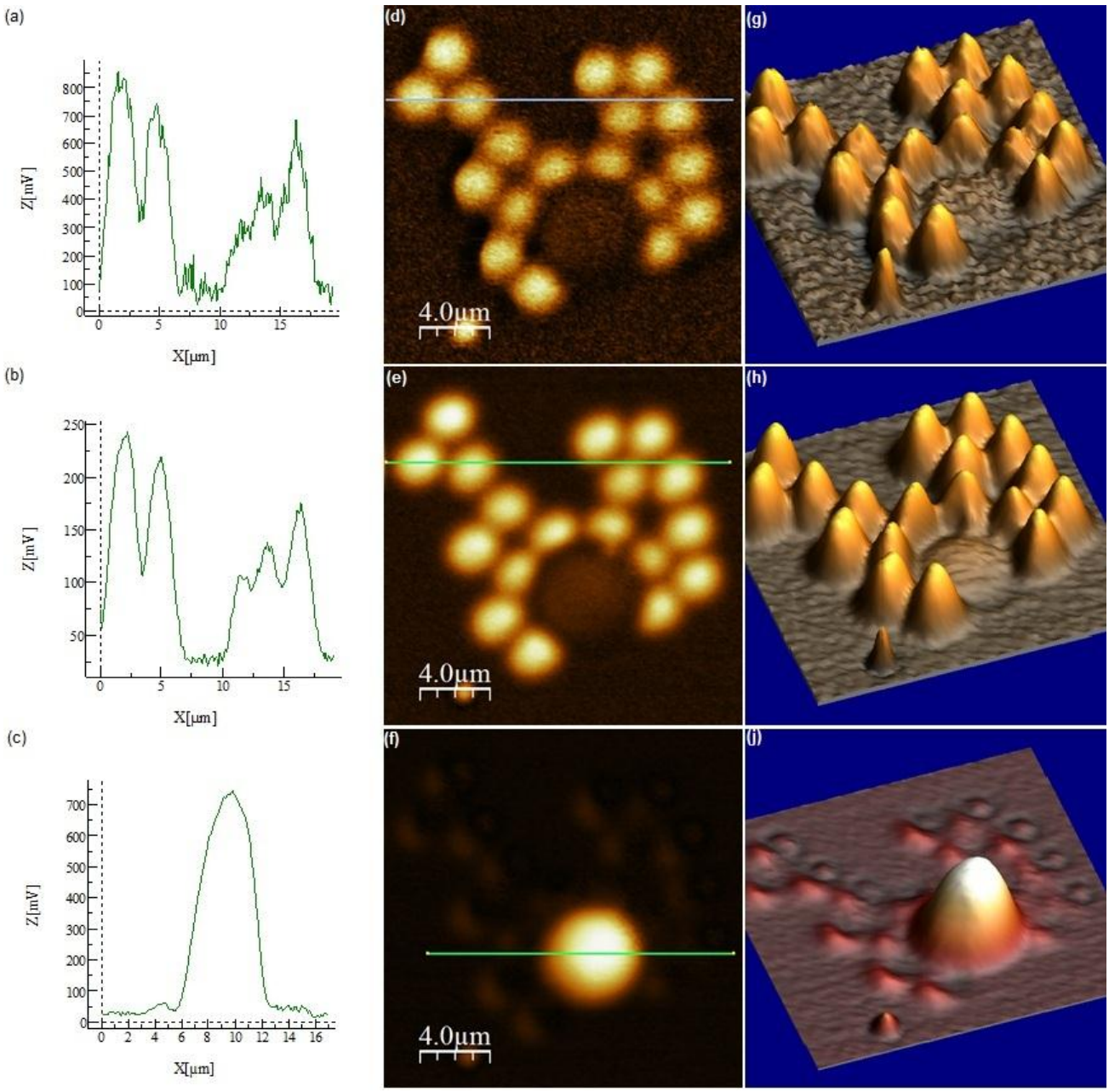

Fig.4.6 (a) SRS 2D profile of PS beads; (b) RIKES 2D profile of PS beads; (c) RIKES 2D profile of PMMA bead; (d) SRS 2D image of PS beads; (e) RIKES 2D image of PS beads; (f) RIKES 2D image of PMMA bead; (g) SRS 3D profile of PS beads; (h) RIKES 3D profile of PS beads; (j) RIKES 3D profile of PMMA bead

Looking at the RIKES images and 3D profiles in Fig.4.6 one can note that tuning the Stokes wavelength to probe the PS, PMMA bead is nearly invisible, and vice versa. This is confirmed looking at the 2D profiles: when scanning in regions without PS beads the signal is close to zero, thus the PMMA contribution is nearly absent. Looking at Fig.4.6 (c) it is immediate to see that away from the PMMA bead the signal is close to zero, even if the bead is closely surrounded by PS beads. This results in an appreciable contrast, granting the expected chemical specificity.

Conclusions

The thesis activity was mainly based on two parallel aspects: a theoretical study of CRS processes and several experiments conducted in the laboratory at Politecnico di Milano, Polo Leonardo.

The theoretical study was structured in a way that, starting from the basis of the non-linear interaction between light and matter, it was possible to derive the most relevant expression for CRS techniques, focusing on the aspects that matter in the experimental work. In particular CARS and SRS have been presented, highlighting pros and cons of both of them, to show the reasons that led us to implement a more complicated technique such as RIKES. Afterwards RIKES has been discussed, first through a mathematical derivation of the main equations representing the signal to be detected, and then through the comparison between three different detection schemes.

The main goals of experimental work were two: designing and building a new laser setup, different from those commonly used for CRS purposes, based on a fiber oscillator, and proving the feasibility of the balanced detection scheme, a well-known technique which has never proved to be applied to RIKES experiments.

The setup, entirely built during this activity, is based on a Er:fiber laser and uses a recently demonstrated spectral compression technique. It generates widely tunable, narrowband, picosecond pulses by a second harmonic generation process from broadband femtosecond pulses. It allowed us to utilize pump pulses with wavelength of 780 nm, powers up to 120 mW and a spectral width of 15 cm^{-1}. The same laser produces Stokes pulses with wavelength tunable from 840 nm to 1100 nm, powers up to 10 mW and spectral width of 18-30 cm^{-1}, thus we were able to tune the system to probe vibrational transitions with frequencies 1000-3500 cm^{-1}, among which the CH stretching region at nearly 3000 cm^{-1}.

This capability to easily tune the Stokes wavelength was exploited to probe CH stretching transitions in methanol, acetone, xylene, and benzene with CARS and SRS measurements, which gave responses consistent to those found in Raman spectra bibliography, with a slight frequency shift in CARS spectra, due to the non-resonant background. The system was used to acquire RIKES spectra of acetone in four different configurations. Finally SRS and RIKES images of PS and PMMA beads on glass substrate were acquired. The balanced detection scheme utilized in RIKES experiments allowed us to reject the noise of the Stokes power, giving clearer images than in SRS case.

In conclusion this activity proved the possibility to build a more compact and cost-effective setup for CRS applications than the most widely used ones, and that with a rather simple detection scheme it is possible to improve the signal to noise ratio in RIKES applications. As a future development, probing of biologically and biomedically relevant samples could be foreseen. These elements could open up a path to apply these techniques not only in a research laboratory, but even in clinical and biomedical application, thanks to the flexibility proved by the setup.

APPENDIX A

Third order nonlinear effects

When approaching to the semi-classical theory of the interaction between matter and light, if the matter is considered as non-linear, before long one runs up against the equation (1.17). If the effect of interest is a third order one it has to be taken into account that the incident electric field is the combination of three different fields, and this complicates a lot the calculation of the corresponding polarization. The goal of this Appendix is to derive a more general expression of the third order non-linear response and briefly describe the main effects driven by such response. A complete description of every nonlinear effect is beyond the purpose of this Appendix.

Recalling equation (1.18) one can observe that the non-linear polarization depends on the incident electric field raised to the third power:

$$P(t) \propto \varepsilon_0 \chi^{(3)} E^3(t) \qquad (A.1)$$

If the electric field now assumes the form given in equation (1.19), it's a polynomial of six terms:

$$E(z,t) = \frac{1}{2}\left(A_1(z,t)e^{i(\omega_1 t - k_1 z)} + A_2(z,t)e^{i(\omega_2 t - k_2 z)} + A_3(z,t)e^{i(\omega_3 t - k_3 z)} + c.c.\right) (A.2)$$

Raising it to the third power it results in a polynomial of 126 terms.

For simplicity it is useful to introduce some substitutions:

$$\begin{cases} a = A_1(z,t)e^{i(\omega_1 t - k_1 z)} \\ b = A_2(z,t)e^{i(\omega_2 t - k_2 z)} \\ c = A_3(z,t)e^{i(\omega_3 t - k_3 z)} \\ a^* = A_1^*(z,t)e^{-i(\omega_1 t - k_1 z)} \\ b^* = A_2^*(z,t)e^{-i(\omega_2 t - k_2 z)} \\ c^* = A_3^*(z,t)e^{-i(\omega_3 t - k_3 z)} \end{cases} \qquad (A.3)$$

Now equation (A.2) can be written as:

$$P = \frac{1}{2}(a + b + c + a^* + b^* + c^*)^3 \qquad (A.4)$$

Solving (A.4) and reordering the terms one obtains:

$$P^3 = \left(a^3 + b^3 + c^3 + a^{*^3} + b^{*^3} + c^{*^3}\right) + 3\left(ab^2 + ac^2 + bc^2 + a^2b + a^2c + b^2c + a^*b^{*^2} + a^*c^{*^2} + b^*c^{*^2} + a^{*^2}b^* + a^{*^2}c^* + b^{*^2}c^*\right) + 6(abc + a^*b^*c^*) + 3\left(a^*b^2 + a^*c^2 + b^*c^2 + a^2b^* + a^2c^* + b^2c^* + ab^{*^2} + ac^{*^2} + bc^{*^2} + a^{*^2}b + a^{*^2}c + b^{*^2}c\right) + 6(a^*bc + ab^*c + abc^* + ab^*c^* + a^*bc^* + a^*b^*c) + 3(a|a|^2 + b|b|^2 + c|c|^2 + a^*|a|^2 + b^*|b|^2 + c^*|c|^2) + 6(b|a|^2 + c|a|^2 + a|b|^2 + c|b|^2 + a|c|^2 + b|c|^2 + b^*|a|^2 + c^*|a|^2 + a^*|b|^2 + c^*|b|^2 + a^*|c|^2 + b^*|c|^2) \qquad (A.5)$$

Each bracket incloses terms that give rise to a specific third order effect. Table 1 summarizes a list of the possible effects. In principle in a crystal with a third order susceptibility all effects are present at once. Some of them are not experimentally appreciable due to the lack of the corresponding phase match condition, to insufficient field intensity, or to screening from stronger effects. Remembering the substitution (A.3), it is easy to observe that the terms *a,b,* and *c* contribute to the outgoing beam (ω_4) with a

factor $+\omega_1, +\omega_2, \text{or } +\omega_3$ respectively, while the terms $a^*, b^*, \text{and } c^*$ contribute with a factor $-\omega_1, -\omega_2, \text{or } -\omega_3$ respectively.

With the help of Table 1, each term in equation (A.5) will be discussed[8].

Non-linear Process	$\mathbf{8P(\omega_4)/\varepsilon_0\chi^{(3)}}$	$\boldsymbol{\omega_4}$
Third Harmonic Generation (THG)	$A_i^3, i = 1,2,3$	$3\omega_1, 3\omega_2, 3\omega_3$
Sum Frequency Generation (SFG)	$3A_iA_j^2\ , i,j = 1,2,3\ \ i \neq j$	$2\omega_1 + \omega_2, 2\omega_1 + \omega_3,$ $2\omega_2 + \omega_3, 2\omega_2 + \omega_1,$ $2\omega_3 + \omega_1, 2\omega_3 + \omega_2$
	$6A_1A_2A_3$	$\omega_1 + \omega_2 + \omega_3$
Frequency Mixing	$3A_i^*A_j^2\ , i,j = 1,2,3\ \ i \neq j$	$2\omega_1 - \omega_2, 2\omega_1 - \omega_3,$ $2\omega_2 - \omega_3, 2\omega_2 - \omega_1,$ $2\omega_3 - \omega_1, 2\omega_3 - \omega_2$
Coherent Stokes and anti-Stokes Raman Scattering (CSRS-CARS)	$6A_i^*A_jA_k\ , i,j,k = 1,2,3\ \ i \neq j \neq k$	$\omega_1 + \omega_2 - \omega_3$ $\omega_1 - \omega_2 + \omega_3$ $-\omega_1 + \omega_2 + \omega_3$
	$6A_i^*A_j^*A_k\ , i,j,k = 1,2,3\ \ i \neq j \neq k$	$\omega_1 - \omega_2 - \omega_3$ $-\omega_1 + \omega_2 - \omega_3$ $-\omega_1 - \omega_2 + \omega_3$
Self-Phase Modulation	$3A_i^2A_i^*\ , i = 1,2,3$	$\omega_1, \omega_2, \omega_3$
Two Beams Coupling	$6A_iA_jA_j^*\ , i,j = 1,2,3\ \ i \neq j$	$\omega_1, \omega_2, \omega_3$

Table 1. Third order non-linear effects

The first group of terms in equation (A.5) and in Table 1 refers to the *third-harmonic generation* process; it is in principle always existing, but in crystals where $\chi^{(2)}$ is different from zero it's almost completely covered by the second-harmonic generation effect. That's because the typical values of $\chi^{(2)}$ are orders of magnitude greater than $\chi^{(3)}$ coefficients found in common crystals. To get a THG signal in those crystals which have an inversion

symmetry, very high intensities are needed, risking to damage the material. Achieving the THG phase matching condition is not simple and usually is preferred to use a sequence of two second order processes to obtain higher order harmonics[7].

The second and the third group of terms refers to the *sum frequency generation* process, which generates many different frequencies, which are every possible sum of the three incoming frequencies, each of them with a different orientation, given by the respective phase matching condition.

The fourth group of terms refers to the *frequency mixing* process. This effect is generated by the *self-diffraction* phenomenon. The first and the second beam interacting in the medium create a diffraction grating because the interference between the two of them has a sinusoidal spatial dependence. The peculiarity of this process is that the first beam is itself diffracted off the grating, so the third beam is the same as the first one (and that gives the second power in the polarization expression). As a result two beams are created at frequencies $\omega_4=2\omega_1-\omega_2$ and $\omega_4=2\omega_2-\omega_1$ and with different wave vectors and thus different directions[7].

The fifth group of terms is the one that gives rise to the so-called *coherent Stokes and anti-Stokes Raman scattering* effects. These are not else than a more general case of *frequency mixing*. In this case there are three different beams interacting, each of them with a

different frequency. This way it's possible to generate any combination of sum/difference of the three beams. Those last two effects make possible to observe the CARS signal.

The *optical Kerr effect* is responsible for the *self phase modulation* which is described by the sixth group of terms in equation (A.5) and in Table 1. These terms are proportional to the field amplitude multiplied by the absolute square of the same field. When a high intensity field interacts with the matter, the matter experiences a variation in the refractive index proportional to the field intensity. This change induces a different phase in the exponential term representing the travelling pulse. Being the instantaneous frequency the derivative of the phase, it can be proved that the following equation is valid:

$$\omega_i(t) = \frac{d\varphi}{dt}(t) \approx \omega_0 - \frac{d(|A(t)|^2)}{dt} \qquad (A.6)$$

The derivative on the right side of equation (A.6) being positive on the positive slope of the pulse causes a decrease in the frequency, or a so-called *red shift*. On the negative slope of the pulse the derivative is negative and there is a *blue shift* in the frequency.

The last effect that can be found in equation (A.5) is the *two-beam coupling*. It can be seen that the outgoing beam has the same frequency of one of the two incoming beams. This effect depends upon the absolute square of the other field, used as a pump. In a particular implementation of this effect, the *polarization gating*, the pump field induces a nonlinear response, which affects the other field, polarized at 45° to the other and weak enough not to induce any non-linear response. The pump creates a nonlinear refractive index change in

the medium that will affect the weak field parallel component. In the medium a nonlinear birefringence is set up, and with sufficient pump intensity and medium length, a full 90° rotation of the weak wave polarization can be achieved. In any case a fraction of the component that is orthogonal to the original weak wave is generated, which can be isolated by using one of the techniques described in Chapter 2. This effect lays at the base of RIKES experiments[7] [8]. The same effect, without any difference in the polarization state of the two beam, lays at the base of SRS experiments.

APPENDIX B

Effects of wave plates and Wollaston prism

In this Appendix the calculations to get a balanced detection out of a configuration with a wave plate, a Wollaston prism and balanced detector will be presented. First of all one should understand how these three devices work, then the overall effects of the three combined will be mathematically proved and explained.

During RIKES experiments λ/2 and λ/4 plates were used. These kind of optical devices alter the polarization state of a light wave travelling in it, by shifting the phase between two perpendicular polarization components of the wave. A typical wave plate is simply a birefringent crystal with carefully chosen orientation and thickness. The crystal is cut so that the optic axis (extraordinary axis) is parallel to the surfaces of the plate. Light polarized along this axis travels through the crystal at a different speed than light with the perpendicular polarization (along the ordinary axis), creating a phase difference. Depending on the material the extraordinary refractive index can be greater or smaller than the ordinary one. The wave plate is characterized by the amount of relative phase, Γ, that it

imparts on the two components, which is related to the birefringence Δn and the thickness L of the crystal by the following formula:

$$\Gamma = \frac{2\pi\Delta nL}{\lambda_0} \qquad (B.1)$$

A quarter-wave (λ/4) plate creates a quarter-wavelength phase shift ($\Gamma = 90°$) and can change linearly polarized light to circular and vice versa by setting the angle between the optic axis of the plate and the linear polarization to 45°. A half-wave (λ/2) plate retards one polarization by a half a wavelength ($\Gamma = 180°$) and it is used to change the direction of linear polarized light by an angle double of the one between the optic axis and the polarization direction.

The Wollaston prism is made up of two right birefringent prisms with perpendicular optic axes. As the light wave goes into the first prism, the two polarization components experience a different refractive index. Then, at the interface of the two prisms, the refractive indeces experienced by the different polarization components change: the component travelling in the first prism along the ordinary axis will travel along the extraordinary one in the second prism, and vice versa. Both of the components experience a refraction with different and opposite angles, so the beams diverge from the prism, giving two polarized beams, with polarization directions orthogonal one to the other.

A balanced detector is a combination of two photodiodes detecting two different beams intensity on two different channels: the *signal* channel and *reference* channel. This kind of

detector has an elaboration stage which calculates the difference between the intensities of the two channels. The overall signal is given by:

$$I \approx R\left(P_{sig} - P_{ref}\right) \qquad (B.2)$$

where R is the transimpedance gain and P_{sig}, P_{ref} are the powers of the signal and the reference beam respectively.

In RIKES experiments a linearly polarized wave, after travelling through the sample in which the other beam induces the birefringence, and thus experiencing a polarization shift, is sent to a wave plate. The goal is to measure the polarization rotation induced by the Kerr effect. After the wave plate the beam is split in the two polarization components by a Wollaston prism and then detected by a balanced detector. To perform this measurement with the balanced detection we need to be sure that without the pump beam (which induces the Kerr effect), the two channels of the detector are balanced. In the following the relation between the signal measured and the initial field amplitude, as well as the right angles which the wave plates should be rotated by will be pointed out.

The following argument will be presented in the most generic way: the incoming beams are not supposed to have a specific polarization state, while in RIKES experiment they were used with controlled polarization states. First the case of a λ/2 plate placed on the detection path will be discussed, then the case of a λ/4 plate.

Considering a generic electric field E, it can be written as a vector sum of two orthogonal polarization components E_x+E_y:

$$\begin{cases} E_x = A_x e^{i(\omega t - kz)} \\ E_y = A_y e^{i(\omega t - kt)} \end{cases} \quad (B.3)$$

where A_i are the field amplitudes. In the following the exponential terms will be neglected, being the frequency and the wavelength always unchanged.

Referring to Fig.B.1 x and y are the axes in the laboratory frame of reference (black lines), while u and v are the axes in the wave plate frame of reference (red lines). First the case of a λ/2 plate will be discussed.

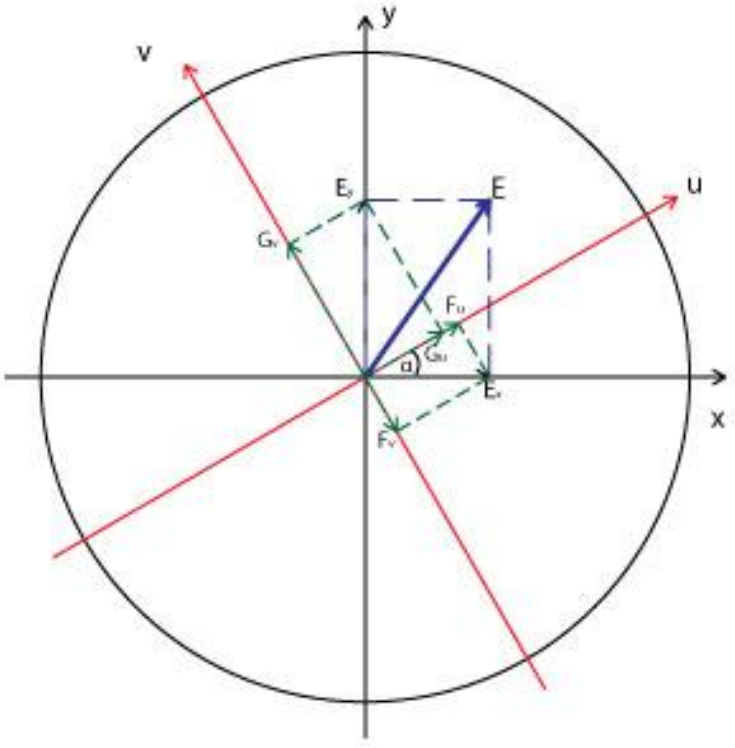

Fig.B.1 Frames of reference and field vectors relevant in balanced detection RIKES

The two vectors described by equations (B.3) are the projections of the field vector E on the x,y set of axes and they can be projected on the u,v set of axes. Calling F_u and F_v the projections of the vector E_x, their expressions can be easily obtained:

$$\begin{cases} F_u = E_x \cos\alpha = A_x \cos\alpha \\ F_v = E_x \sin\alpha = A_x \sin\alpha \end{cases} \qquad (B.4)$$

being α the angle between the x axis and the u axis, i.e. the angle between the optic axis of the wave plate and the horizontal plane in the laboratory.

Similarly also E_y can be projected, giving rise to the following terms:

$$\begin{cases} G_u = E_x \sin\alpha = A_y \sin\alpha \\ G_v = E_x \cos\alpha = A_y \cos\alpha \end{cases} \qquad (B.5)$$

The λ/2 wave plate delays one of the two components by π. Let's assume that the v-components are delayed, thus one obtains the following expressions:

$$F_v = A_x e^{i\pi} \sin\alpha \qquad (B.6)$$

$$G_v = A_y e^{i\pi} \cos\alpha \qquad (B.7)$$

On each axis in the frame of reference of the wave plate lay two vectors, which can be added merging into vectors H_u and H_v.

In Fig.B.1 it is possible to notice that vector F_v is negative, thus the expression for sum vectors will be:

$$\begin{cases} H_u = F_u + G_u \\ H_v = -F_v + G_v \end{cases} \quad (B.8)$$

Substituting previous equations into (B.8) one obtains:

$$\begin{cases} H_u = A_x \cos\alpha + A_y \sin\alpha \\ H_v = -A_x e^{i\pi} \sin\alpha + A_y e^{i\pi} \cos\alpha \end{cases} \quad (B.9)$$

After propagating through the wave plate the beam is sent in the Wollaston prism, which is oriented in the same way as the frame of reference of the laboratory, thus one has to project the vectors described by equations (B.9) on the *x*,*y* set of axes again.

With simple geometrical calculations one can obtain the following set of equations which gives the expression of the resulting field vectors I_x and I_y going out the Wollaston prism:

$$\begin{cases} J_x = H_u \cos\alpha - H_v \sin\alpha \\ J_y = H_u \sin\alpha + H_v \cos\alpha \end{cases} \quad (B.10)$$

Substituting equations (B.9) into (B.10):

$$\begin{cases} J_x = A_x \cos^2\alpha + A_y \sin\alpha \cos\alpha + A_x e^{i\pi} \sin^2\alpha - A_y e^{i\pi} \sin\alpha \cos\alpha \\ J_y = A_x \sin\alpha \cos\alpha + A_y \sin^2\alpha - A_x e^{i\pi} \sin\alpha \cos\alpha + A_y e^{i\pi} \cos^2\alpha \end{cases} \quad (B.11)$$

J_x and J_y are now the fields going to the two different channels of the balanced detector.

Calling back to mind Euler's identity ($e^{i\pi} + 1 = 0$) after some trigonometric calculations, it is possible to write set of equations (B.11) as follows:

$$\begin{cases} J_x = A_x \cos 2\alpha + A_y \sin 2\alpha \\ J_y = A_x \sin 2\alpha - A_y \cos 2\alpha \end{cases} \qquad (B.12)$$

In order to perform a balanced detection measurement one has first to align the system without the birefringence-inducing beam, in a way that the combination of the wave plate and the Wollaston prism give a perfectly balanced signal. To obtain this balancing the initial component E_x, once rotated by the wave plate and projected again on the two axes in the laboratory frame by the Wollaston prism, should give two equal vectors. This condition is satisfied when the intensities of the fields F_u and F_v are equal. The same has to happen with the initial component E_y, giving the condition that the intensities of G_u and G_v have to be equal.

To accomplish these conditions it turns out that one has to solve the following equation:

$$\cos^2 2\alpha = \sin^2 2\alpha \qquad (B.13)$$

Solving equation (B.13) the right value of α it turns to be: $\alpha = \pm\frac{\pi}{8} + k\frac{\pi}{2}$.

Imposing the previous condition with the positive value of α is finally possible to obtain the expression of the difference between the intensity of the two fields, which is the value that is detected:

$$\Delta I = |J_x|^2 - |J_y|^2 = \frac{1}{2}\left(|A_x|^2 + |A_y|^2 + 2Re\{A_x A_y^*\}\right) - \frac{1}{2}\left(|A_x|^2 + |A_y|^2 - 2Re\{A_x A_y^*\}\right)$$
$$= 2Re\{A_x A_y^*\} \qquad (B.14)$$

Equation (B.14) shows the meaning of the detected signal, and starting from this equation, in paragraph 2.3 it is shown which tensor element of the susceptibility is possible to probe.

When the beam is propagating through a λ/4 plate the calculations are similar, but instead of delaying the *v* component by π, the wave plate induces a delay of π/2. While F_u and G_u are the same as in (B.4) and (B.5), in this case F_v and G_v assume the following expressions:

$$F_v = A_x e^{i\pi/2} \sin\alpha \qquad (B.15)$$

$$G_v = A_y e^{i\pi/2} \cos\alpha \qquad (B.16)$$

Being equations (B.8) and (B.10) still valid, with few mathematical calculations one can obtain:

$$\begin{cases} J_x = A_x \cos^2\alpha + A_y \sin\alpha\cos\alpha + A_x e^{i\pi/2} \sin^2\alpha - A_y e^{i\pi/2} \sin\alpha\cos\alpha \\ J_y = A_x \sin\alpha\cos\alpha + A_y \sin^2\alpha - A_x e^{i\pi/2} \sin\alpha\cos\alpha + A_y e^{i\pi/2} \cos^2\alpha \end{cases}$$
$$(B.17)$$

As in the previous case one has to verify that the intensities of the rotated components of one initial field component are equal, and then the same for the other. This results in the following equation:

$$(\cos^2\alpha - \sin^2\alpha)^2 = 0 \qquad (B.18)$$

Solving equation (B.18) one obtains the right angle at which the λ/4 wave plate should be tilted in order to obtain the balancing: $\alpha = \pm\frac{\pi}{4} + k\frac{\pi}{2}$.

Keeping the positive solution for α, similarly to equation (B.14), after few calculations, this time the measured signal, i.e. the difference between the intensities of the two channels when the beam propagates through a λ/4 plate is:

$$\Delta I = 2Im\{A_x A_y^*\} \qquad (B.19)$$

REFERENCES

1. G. L. Eesley, “Coherent Raman spectroscopy”, *J. QUANT. SPECTROSC. RADIAT. TRANSFER.* **Vol. 22**, 507-576 (November 17, 1978)

2. Christian W. Freudiger, Wei Min, Brian G. Saar, Sijia Lu, Gary R. Holtom, Chengwei He, Jason C. Tsai, Jing X. Kang, X. Sunney Xie, “Label-free biomedical imaging with high sensitivity by stimulated Raman scattering microscopy”, *SCIENCE*, **Vol. 322**, 1857-1861 (December 19, 2008)

3. A. Gambetta, V. Kumar, G. Grancini, D. Polli, R. Ramponi, G. Cerullo, M. Marangoni, “Fiber-format stimulated-Raman-scattering microscopy from a single laser oscillator, *OPTICS LETTERS*, **Vol. 35, No. 2,** 226-228 (January 15, 2010)

4. Conor L. Evans, X. Sunney Xie, “Coherent anti-Stokes Raman scattering: chemical imaging for biology and medicine”, *ANNUAL REVIEW OF ANALYTICAL CHEMISTRY*, **Vol. 1,** 883-909 (October 14, 2008)

5. M. Marangoni, A. Gambetta, C. Manzoni, V. Kumar, R. Ramponi, G. Cerullo, “Fiber-format CARS spectroscopy by spectral compression of femtosecond pulses

from a single laser oscillator", OPTICS LETTERS, **Vol. 34, No. 21,** 3262-3264 (November 1, 2009)

6. Christian W. Freudiger, Maarten B. J. Roeffaers, Xu Zhang, Brian G. Saar, Wei Min, X. Sunney Xie, "Optical heterodyne-detected Raman-induced Kerr effect (OHD-RIKE) microscopy", *THE JOURNAL OF PHYSICAL CHEMISTRY B,* **Vol. 115, Issue: 18,** 5574-5581 (April 19, 2011)

7. Rick Trebino, John Buck, "Nonlinear optics"

8. Mansoor Sheik-Bahae, Micheal P. Hasselbeck, "Third order optical nonlinearities", *HANDBOOK OF OPTICS*

9. V. Kumar, M. Casella, E. Molotokaite, D. Polli, G. Cerullo, M. Marangoni, "Coherent Raman spectroscopy with a fiber-format femtosecond oscillator"

10. G. Krauss, T. Hanke, A. Snell, D. Träutlein, A. Leitenstorfer, R. Selm, M. Winterhalder, A. Zumbusch, "Compact coherent anti-Stokes Raman scattering microscope based on a picosecond two-color Er:fiber laser system", *OPTICS LETTERS,* **Vol. 34, No. 18,** 2847-2849 (September 15, 2009)

11. F. Ganikhanov, S. Carrasco, X. S. Xie, M. Katz, W. Seitz, D. Kopf, "Broadly tunable dual-wavelength light source for coherent anti-Stokes Raman scattering microscopy", *OPTICS LETTERS,* **Vol. 31, No. 9,** 1292-1294 (May 1, 2006)

12. E. O. Potma, D. J. Jones, J. X. Cheng, X. S. Xie, J. Ye, "High-sensitivity coherent anti-Stokes Raman scattering microscopy with two tightly synchronized picosecond lasers", *OPTICS LETTERS,* **Vol. 27, No. 13,** 1168-1170 (July 1, 2002)

13. A. Zumbusch, G. R. Holtom, X. S. Xie, “Three-dimensional vibrational imaging by coherent anti-Stokes Raman scattering”, *PHYSICAL REVIEW LETTERS,* **Vol. 82, No. 20,** 4142-4145 (May 17, 1999)

14. M. Marangoni, D. Brida, M. Quintavalle, G. Cirmi, F. M. Pigozzo, C. Manzoni, F. Baronio, A. D. Capobianco, G. Cerullo, “Narrow-bandwidth picosecond pulses by spectral compression of femtosecond pulses in a second-order nonlinear crystal”, *OPTICS EXPRESS,* **Vol. 15, No. 14,** 8884-8891 (July 9, 2007)

15. Y. S. Yoo, D. H. Lee, H. Cho, “Differential two-signal picosecond-pulse coherent anti-Stokes Raman scattering imaging microscopy by using a dual-mode optical parametric oscillator”, *OPTICS LETTERS,* **Vol. 32, No. 22,** 3254-3256 (November 15, 2007)

16. F. Ganikhanov, C. L. Evans, B. G. Saar, X. S. Xie, “High-sensitivity vibrational imagin with frequency modulation coherent anti-Stokes Raman scattering (FM CARS) microscopy”, *OPTICS LETTERS,* **Vol. 31, No. 12,** 1872-1874 (June 15, 2006)

17. E. O. Potma, C. L. Evans, X. S. Xie, “Heterodyne coherent anti-Stokes Raman scattering (CARS) imaging”, *OPTICS LETTERS,* **Vol. 31, No. 2,** 241-243 (January 15, 2006)

18. M. Jurna, J. P. Korterik, C. Otto, H. L. Offerhaus, “Shot noise limited heterodyne detection of CARS signals”, *OPTICS EXPRESS,* **Vol. 15, No. 23,** 15207-15213 (November 12, 2007)

19. E. R. Andresen, S. R. Keiding, E. O. Potma, “Picosecond anti-Stokes generation in a photonic-crystal fiber for interferometric CARS microscopy”, *OPTICS EXPRESS,* **Vol. 14, No. 16,** 7246-7251

20. M. Jurna, J. P. Korterik, C. Otto, J. L. Herek, H. L. Offerhaus, “Background free CARS imaging by phase sensitive heterodyne CARS”, *OPTICS EXPRESS,* **Vol. 16, No. 20,** 15863-15869

21. H. Kano, H. Hamaguchi, “Femtosecond coherent anti-Stokes Raman scattering spectroscopy using supercontinuum generated from a photonic crystal fiber”, *APPLIED PHYSICS LETTERS,* **Vol. 85, No. 19,** 4298-4300 (November 8, 2004)

22. T. W. Kee, M. T. Cicerone, “Simple approach to one-laser, broadband coherent anti-Stokes Raman scattering microscopy”, *OPTICS LETTERS,* **Vol. 29, No. 23,** 2701-2703 (December 1, 2004)

23. B. von Vacano, L. Meyer, M. Motzkus, “Rapid polymer blend imaging with quantitative broadband multiplex CARS microscopy”, *JOURNAL OF RAMAN SPECTROSCOPY,* **Vol. 38,** 916-926 (April 11, 2007)

24. V. Kumar, R. Osellame, R. Ramponi, G. Cerullo, M. Marangoni, “Background-free broadband CARS spectroscopy from a 1-MHz ytterbium laser”, *OPTICS EXPRESS,* **Vol. 19, No. 16,** 15143-15148 (August 1, 2011)

25. P. Nandakumar, A. Kovalev, A. Volkmer, “Vibrational imaging based on stimulated Raman scattering microscopy”, *NEW JOURNAL OF PHYSICS,* **Vol. 11, Ref. 033026,** 1-9 (2009)

26. B. G. Saar, C. W. Freudiger, J. Reichman, C. M. Stanley, G. R. Holtom, X. S. Xie, “Video-rate molecular imaging in vivo with stimulated Raman scattering”, *SCIENCE*, **Vol. 330,** 1368-1370 (December 3, 2010)

27. D. W. McCamant, P. Kukura, S. Yoon, R. A. Mathies, “Femtosecond broadband stimulated Raman spectroscopy: Apparatus and methods”, *REVIEW OF SCIENTIFIC INSTRUMENTS*, **Vol. 75, No. 11,** 4971-4980 (November 2004)